STUDY II, The Bunching and Cooling Sections

E. Black[1], D. Elvira[1], D. Kaplan[2], R. Fernow*, J. Gallardo*,
M. A. Green#, P. Lebrun[1], A. Moretti[1], D. Neuffer[1], J. Norem[3],
D. Li#, R. Palmer*, R. Rimmer#, A. Tollestrup[1],
[1]Fermilab, Batavia, Ill 60150,USA
[2]IIT, Chicago, Ill, USA
[3]Argone Natl. Lab., Ill, USA
*BNL, Upton, NY 11973, USA
#LBNL, Berkeley, CA 94720, USA

March 9, 2001

Abstract

The Buncher and sFOFO cooling channel are introduced and described. Performance, systematic errors and tolerances are discussed. These are the section 12 and 13, respectively, in the Feasibility II study document.

1 The Buncher and Matching section from the Induction Linac

After the energy spread of the beam has been reduced in the induction linacs the muons are distributed continuously over a distance of around 100 m. It is then necessary to form the muons into a train of bunches prior to cooling and subsequent acceleration. First an 11 m long magnetic lattice section is used to gently transform the beam from the approximately uniform solenoidal field used in the induction linacs to the so called "super-FOFO", or sFOFO, lattice used in the remainder of the front end. This is followed by the 55 m long *rf* buncher itself, which consists of *rf* cavity sections interspersed with drift regions. The two functions of this section are perfomed sequentially for design simplicity. There is a significant advantage in using the same lattice in the buncher section as in the following cooling region since it avoids adding another complicated 6-dimensional matching section.

Two distinct computer codes were used to simulate this buncher and the cooling channel: ICOOL[5] and Geant4[6]. There is no shared code between the two programming environments, FORTRAN for ICOOL and C++ for Geant4. The Geant4 implementation was based solely on the parameters listed below. After optimization of the matching sections and minor clarifications, good agreement

was obtained, as shown in the performance section. Based on this successful comparison, the more demanding magnet alignment tolerance study was done in the generic 3D code, i.e. Geant4.

1.1 Matching section

The goal of the matching section is to smoothly transform the muon beam from the 1.25 T approximately uniform focusing field to the 2 T alternating polarity s-FOFO lattice. The 4 % rms momentum spread entering the matching section is relatively small, so chromatic corrections are less critical than in the mini-cooling field reversal. Table 1 gives coil dimensions and current densities for the solenoid magnets used in the match.

Table 1: Matching section magnets

z	dz	r	dr	j
m	m	m	m	A/mm^2
0.358	1.375	0.300	0.100	-9.99
1.733	0.330	0.300	0.110	-15.57
2.446	0.187	0.330	0.330	-33.40
2.963	0.187	0.330	0.330	35.19
4.008	0.330	0.770	0.110	67.41
5.146	0.187	0.330	0.330	43.75
5.663	0.187	0.330	0.330	-43.75
6.708	0.330	0.770	0.110	-66.12
7.896	0.187	0.330	0.330	-43.75
8.413	0.187	0.330	0.330	43.75
9.458	0.330	0.770	0.110	66.12
10.646	0.187	0.330	0.330	43.75

The magnet configuration at the beginning of the section, the axial magnetic field on-axis, and the beta function for three momenta are shown in Fig. 1. The magnetic lattice goes from a series of constant radius solenoids to a s-FOFO cell structure consisting of small radius coils at each end of a cell and a large radius coil in the middle. Four magnets in the transition region have non-standard current densities. The axial magnetic field in a cell peaks symmetrically near the two ends and has a smaller secondary peak in the middle. The beta function across the match is similar for the three particles shown, which vary in momentum in steps of 7.5 % from 185 to 215 MeV/c.

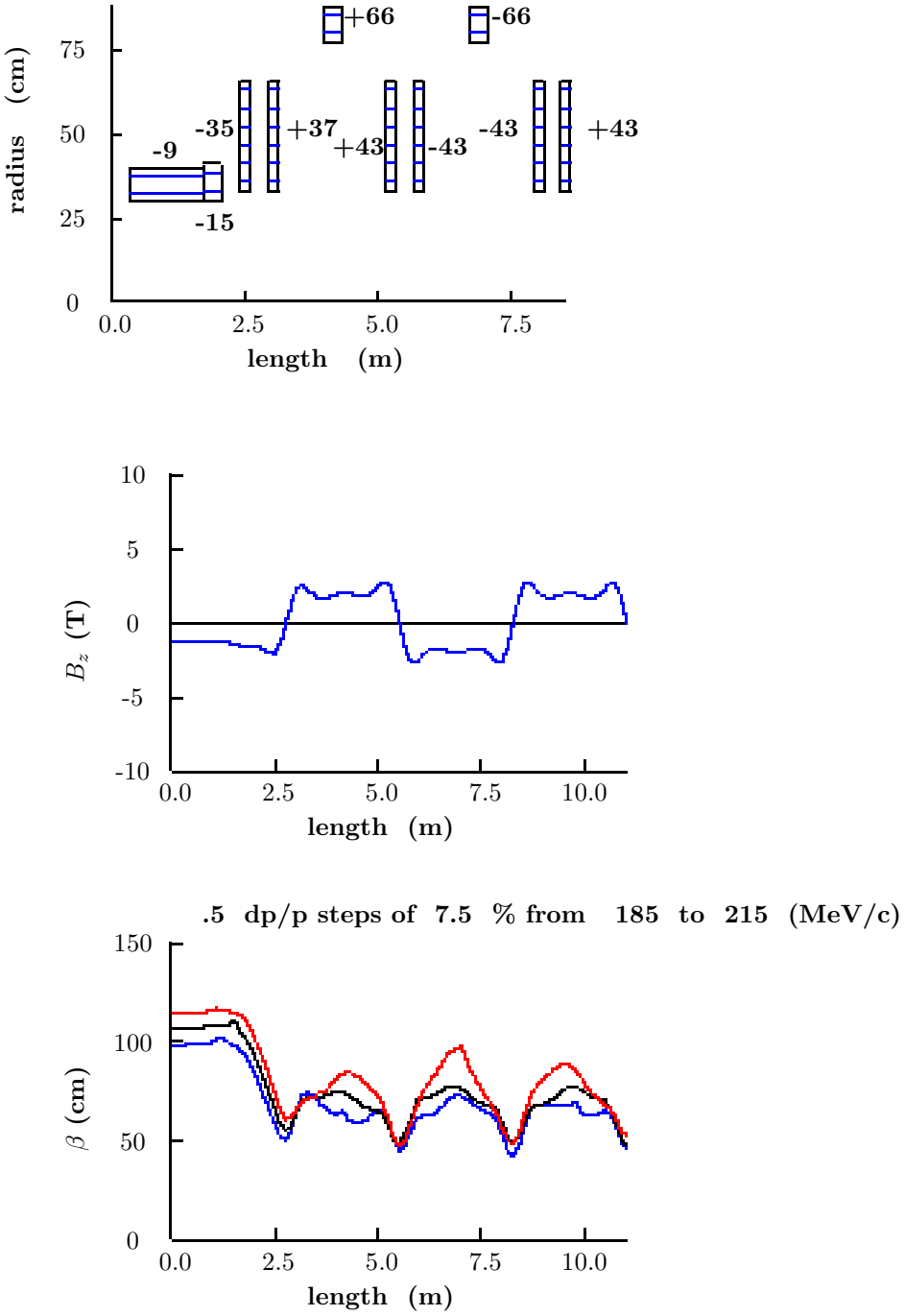

Figure 1: Magnet configuration; axial magnetic field; beta function.

1.2 Buncher section

The design principles for the lattice and details concerning the *rf* and other technical components for the buncher section will be described later. Only the beam dynamics and performance will be described here. The buncher magnetic lattice is identical to that used in the first cooling section. It contains *rf* cavities in selected lattice cells and no absorbers. The main *rf* frequency was chosen to be 201.25 MHz in the front end, so that the beam would fit radially inside the cavity aperture and because power sources and other technical components are available at this frequency. The 201.25 MHz cavities are placed at the high beta locations in the lattice, just as in the cooling section. Harmonic cavities running at 402.5 MHz are placed at beta minimum locations, where hydrogen absorbers are located in the cooling section.

The buncher encompasses 20 lattice cells, each 2.75 m long. Maximum bunching efficiency was obtained by breaking the region into three *rf* stages separated by drift regions. The locations and lengths of the buncher components are given in Table 2.

Table 2: *rf* buncher component locations

	length m	frequency MHz	phase degree	gradient MV/m
harmonic *rf*	.186	402.5	180	6.4
space	.443			
rf	4 × .373	201.25	0	6.4
space	.443			
harmonic *rf*	.186	402.5	180	6.4
drift 1	10 × 2.75			
harmonic *rf*	.186	402.5	180	6
space	.443			
rf	4 × .373	201.25	0	6
space	.443			
harmonic *rf*	2 × .186	402.5	180	6
space	.443			
rf	4 × .373	201.25	0	6
space	.443			
harmonic *rf*	.186	402.5	180	6
drift 2	3 × 2.75			
space	.629			
rf	4 × .373	201.25	12	8
space	.629			
space	.629			
rf	4 × .373	201.25	12	8
space	.629			
drift 3	2 × 2.75			

Second harmonic (402.5 MHz) cavities are used at the entrance and exit of the first and second stages to linearize the shape of the *rf* pulse. All cavities are assumed to have thin Be windows at each end. They are modelled in the simulation codes as perfect TM_{010} pillboxes. The window radii and thicknesses are given in Table (REFER TO TABLE 18.D HERE).

The electric field gradient is gradually raised in the buncher from 6 to 8 MV/m. A long drift is provided after the first stage to allow the particles to begin overlapping in space.

The following Fig. 2 shows the momentum-time distributions at the start, and after each of the three buncher stages. Distributions are also shown at the ends of the first and second cooling stages. In the last three distributions, ellipses are drawn indicating the approximate acceptance of the cooling channel.

It can be seen that at the end of the buncher, most, but not all, particles are within the approximately elliptical bucket. About 25 % are outside the bucket and are lost relatively rapidly, and another 25 % are lost more slowly as the longitudinal emittance rises from straggling and the negative slope of the energy loss with energy.

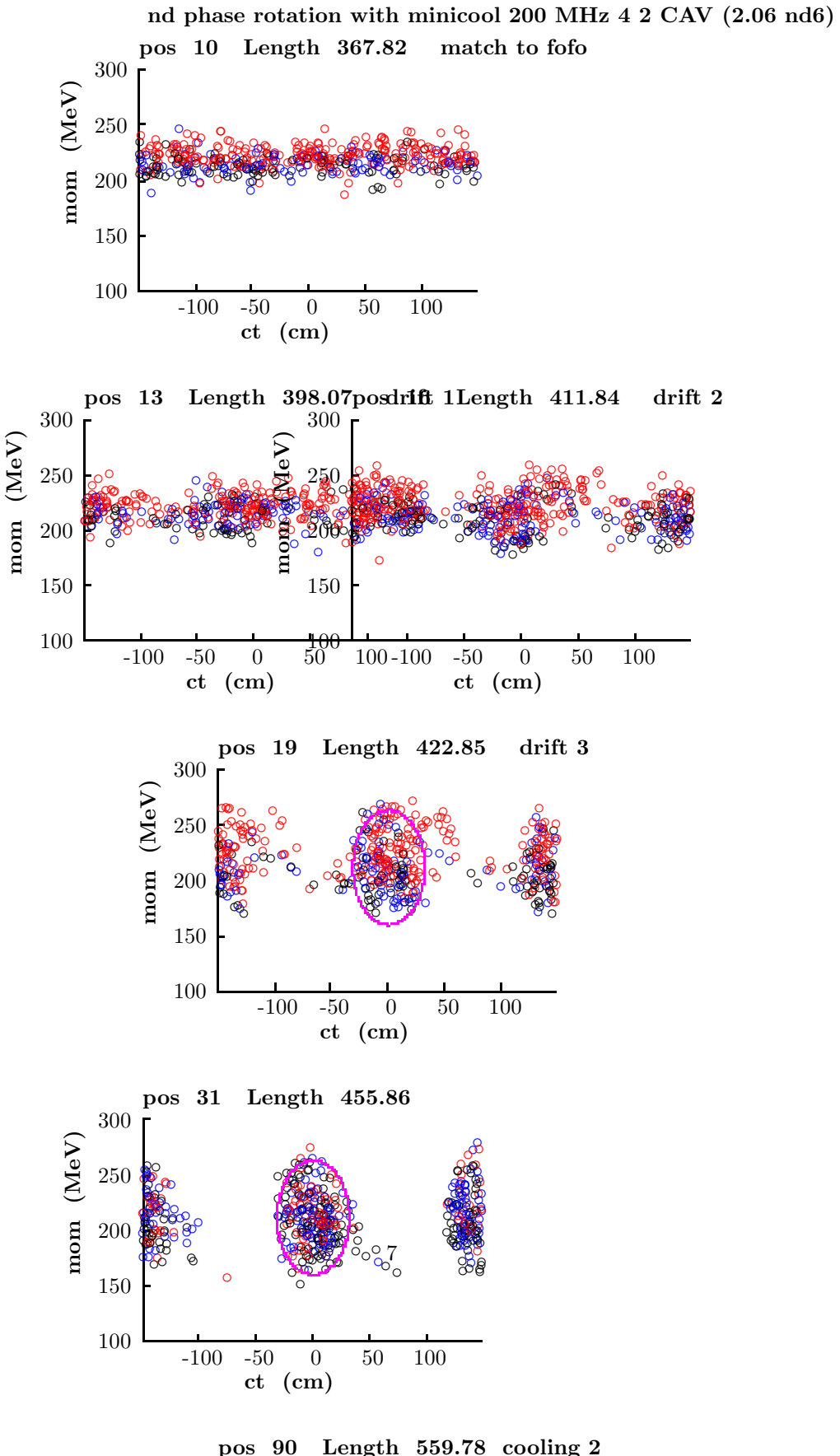
nd phase rotation with minicool 200 MHz 4 2 CAV (2.06 nd6)
pos 10 Length 367.82 match to fofo
pos 13 Length 398.07
drift 1
Length 411.84 drift 2
pos 19 Length 422.85 drift 3
pos 31 Length 455.86
pos 90 Length 559.78 cooling 2
mom (MeV)
ct (cm)
300
250
200
150
100
-100
-50
0
50
100
7

1.3 Longitudinal-transverse correlation

A significant coupling develops in this front end lattice, including the induction linac, between a particle's longitudinal and transverse motions. This coupling develops because particles with different transverse displacements or angular divergences take different amounts of time to move axially down the solenoidal lattice. They thus arrive at the cavities at different points in the *rf* cycle, thereby obtaining different acceleration and different longitudinal and transverse focusing.

The correlation can be expressed as

$$p = p_o + CA^2 \tag{1}$$

where C is the correlation coefficient and the transverse amplitude is

$$A^2 = \frac{r^2}{\beta_\perp^2} + \theta^2 \tag{2}$$

Figure 3 shows that there is little correlation between momentum and angular momentum after the induction linacs, indicating that the field reversal is correctly located.

The magnitude of the momentum-amplitude correlation is seen to be 0.7. This is a higher value than the correlation of 0.45 that would be obtained without the mini-cooler. Ideally the correlation should be such that forward velocity in the following lattice is independent of transverse amplitude. A value of approximately 1.1 would be required for this.

2 The Ionization Cooling Channel

The *rms* transverse emittance of the muon beam emerging from the induction linac must be reduced to at least $\approx$ 2 mm rad (normalized) in order to fit in the downstream accelerators, and be contained in the storage rings. Ionization cooling is currently our only feasible option[1]. The cooling channel described below, as well as the one described in the appendix, are based on extensive theoretical studies and computer simulations performed in the same context of our previous studies[2, 1, 3, 4].

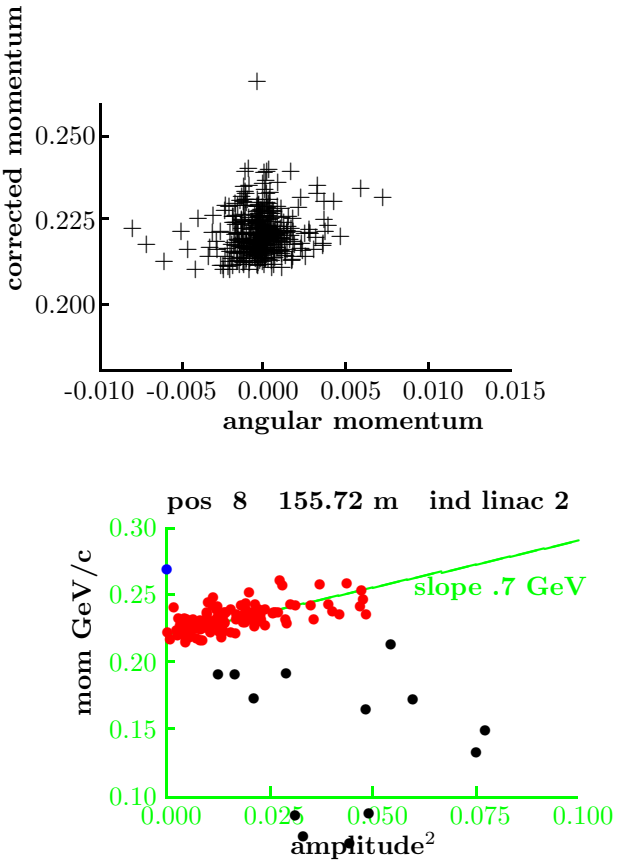

Figure 3: (a) Correlation between momentum and angular momentum; (b) correlation between longitudinal momentum and transverse amplitude.

2.1 Principle of ionization cooling

In ionization cooling the beam loses both transverse and longitudinal momentum by ionization energy loss while passing through the absorber. The longitudinal momentum is then restored to the beam in accelerating cavities. This sequence, repeated many times, results in a reduction of the angular spread and thereby reduces the transverse emittance. Ionization cooling is limited by multiple Coulomb scattering (MSC) in these absorbers. To minimize this effect, one must have rather strong focusing at the absorber, with $\beta_{\perp,min} \approx 0.4$ to 0.2 m at a momentum of 200 MeV/c .

Strong solenoidal fields are used for this purpose. Weak focusing at the absorber, i.e. too large $\beta_\perp$ at the absorbers, leads to excessive emittance growth due to MSC. Too strong focusing is not only hard to achieve for such large aperture beam transports, but can also be detrimental to the 6D beam dynamics. As the angles, or beam divergence, get too large, the longitudinal velocity decreases too much, leading to the wrong longitudinal-transverse correlation factor and thereby resulting in unacceptable growth of the longitudinal emittance. Choosing the right range of $\beta_{\perp,min}$ and the operating momentum is the key to a successful design[1, 4].

The approximate equation for transverse cooling in a step ds along the particle's orbit is [2]

$$\frac{d\epsilon_N}{ds} = -\frac{1}{\beta^2}\frac{dE_\mu}{ds}\frac{\epsilon_N}{E_\mu} + \frac{\beta_\perp (0.014GeV)^2}{2\beta^3 E_\mu m_\mu L_R}, \tag{3}$$

where β is the normalized velocity, E_μ is the total energy, m_μ is the muon mass, ϵ_N is the normalized transverse emittance, $\beta_\perp$ is the betatron function at the absorber, dE_μ/ds is the energy loss per unit length, and L_R is the radiation length of the material. The betatron function is determined by the strengths of the elements in the focusing lattice. Together with the beam emittance this function determines the local size and divergence of the beam. Note that the energy loss dE_μ/ds is defined here as a positive quantity, unlike the convention often used in particle physics. The first term in this equation is the cooling term, and the second describes the heating due to multiple scattering. The heating term is minimized if $\beta_\perp$ is small (strong-focusing) and L_R is large (a low-Z absorber).

The minimum, normalized transverse emittance that can be achieved for a given absorber in a given focusing field is reached when the cooling rate equals the heating rate in Eq. 12

$$\epsilon_{N,min} = \frac{\beta_\perp (14MeV)^2}{2\beta m_\mu \frac{dE_\mu}{ds} L_R} \tag{4}$$

For a relativistic muon in liquid hydrogen with a betatron focusing value of 8 cm, which corresponds roughly to confinement in a 15 T solenoidal field, the minimum achievable emittance is about 340 mm-mrad.

The equation for energy spread is

$$\frac{d(\Delta E_\mu)^2}{ds} = -2\,\frac{d\left(\frac{dE_\mu}{ds}\right)}{dE_\mu}\langle(\Delta E_\mu)^2\rangle + \frac{d(\Delta E_\mu)^2_{\text{stragg.}}}{ds} \tag{5}$$

where the first term describes the cooling (or heating) due to energy loss, and the second term describes the heating due to straggling. ΔE_μ is the rms spread in the energy of the beam.

Ionization cooling of muons seems relatively straightforward in theory, but will require simulation studies and hardware development for its optimization. There are practical problems in designing lattices that can transport and focus the large emittance beam. There will also be effects from space charge and wake fields.

We have developed a number of tools for studying the ionization cooling process. First, the basic theory was used to identify the most promising beam properties, material type and focusing arrangements for cooling. Given the practical limits on magnetic field strengths, this gives an estimate of the minimum achievable emittance for a given configuration. Next several tracking codes were either written or modified to study the cooling process in detail. These codes use Monte Carlo techniques to track particles one at a time through the cooling system. The codes attempt to include all relevant physical processes to some degree, (e.g. energy loss, straggling, multiple scattering) and use Maxwellian models of the focusing fields.

2.2 The concept of the tapered sFOFO cooling Channel

.

The solenoidal field should not be kept constant during the entire cooling stage. The transverse momentum of each particle will decrease, while the position of the Larmor center will not, causing the net total angular momentum of the beam to grow. One must flip the field, while maintaining good focusing throughout the beam transport and low $\beta_\perp$ at the absorbers. One of the simplest solutions, based on the FOFO lattice, is to vary the field sinusoidally. The transverse motion in such a lattice can be characterized by the betatron resonances, near which the motion is unstable. The operating, stable, region is between the 2π and π phase advance per half-period.

The sFOFO lattice[15] is also based on the use on alternating solenoids, but is a bit more complicated. We add a second harmonic to the simple sinusoidal field, producing the axial field shown in figure 5. As in the FOFO case, the longitudinal field vanishes at the $\beta_{\perp,min}$ position, located at the center of the absorber. This is accomplished by two short "focusing" coils running in opposite polarity. However, unlike in the FOFO case, the field decreases and flattens at $\beta_{\perp,max}$, due to a "coupling" coil located around the Linac. Thus, the transverse beam dynamics is strongly influenced by the solenoidal field profile on-axis and by the desired range of momentum acceptance. It is important to note that a geometrical cell in this lattice occupies a half period of the solenoidal magnetic field.

This sFOFO lattice has several advantages over the FOFO:

- The betatron resonances are usually considered a nuisance, since they inevitably induce an unstable motion. However, in this case they give us strong, equal focusing strength across the relevant momentum range, if we operate between the two 2π (low momentum) and π (high momentum) resonances. This is illustrated in Fig. 6 and Fig. 4. Within this (albeit limited) momentum range transverse motion is stable.

- For a given $\beta_{\perp,min}$, the sFOFO period length is longer than in the FOFO case, allowing longer absorbers and linac regions per lattice cell, thereby reducing the relative multiple scattering from the windows. It also gives us a bit more room for all the components for a fixed absorber length.

- The focusing coils can be located above the absorbers, right next to the linac. Since the *rf* cavities have a much larger outer diameter than the absorbers, this arrangement allows us to reduce considerably the diameter of these high field magnets and thereby reduce their cost.

For a given lattice period length, one can adjust independently the location of the two betatron resonances, or, conversely, the nominal operating momentum and the $\beta_{\perp,min}$ at that momentum. By adjusting these two parameters, we can keep the $\beta_\perp$ symmetric about the required nominal momentum, and independently reduce the central $\beta_\perp$ value. However, this is true only over a limited momentum range. As we decrease the coupling field, the momentum

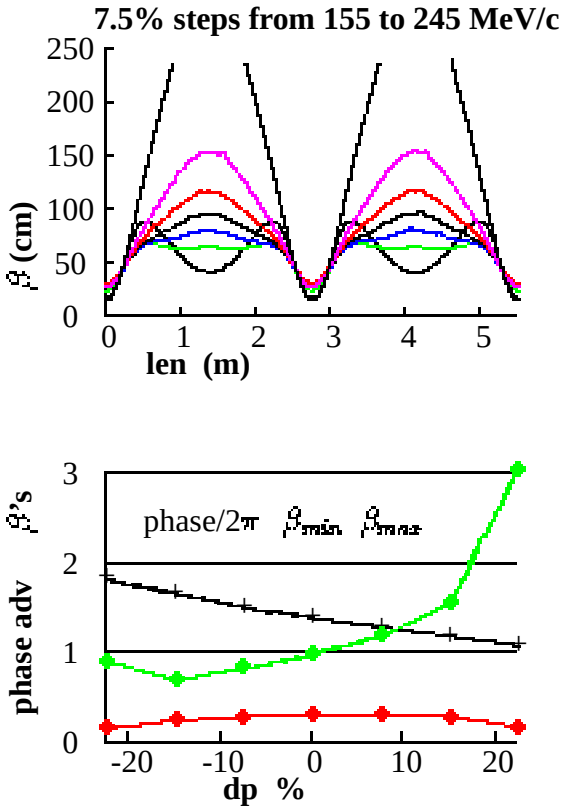

Figure 4: (a) Beta functions in the (1,3) cooling lattice section; (b) phase advance as function of momentum spread.

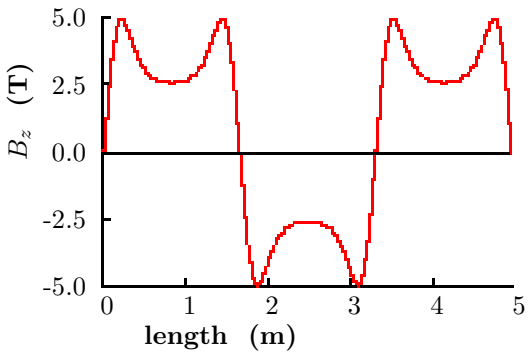

Figure 5: The longitudinal component of the magnetic field, B_z, on axis, for the sFOFO lattice.

acceptance will shrink as the π and 2π resonance move closer to the nominal momentum. At this point, we are forced to change the lattice period.

This brings us to the second improvement over the FOFO channel used in the previous feasibility study: $\beta_{\perp,min}$ can be "tapered" down. One can slowly increase the focusing strength at a fixed operating momentum, keeping a reasonable momentum acceptance. At a fixed $\beta_{\perp,min}$, as the cooling progresses, the *rms* angle would decrease. The cooling rate would then also decrease because the heating term due to multiple scattering becomes relatively significant. By slowly increasing the focusing strength, (decreasing $\beta_{\perp,min}$), one tends to maintain large *rms* angles at the absorbers ($\sigma_{x'} = \sigma_{y'} \approx 0.1$ rad.).

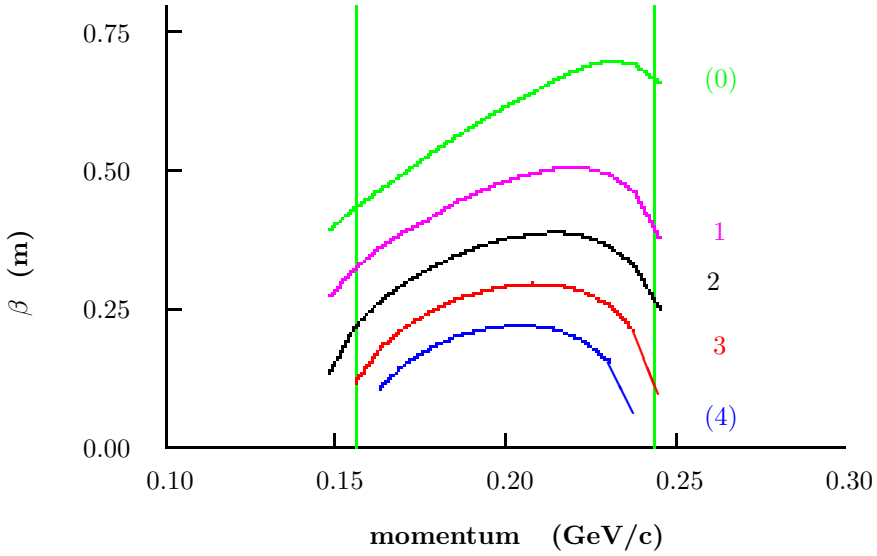

Figure 6: The $\beta_\perp$ function, versus momentum, for the six sFOFO lattices described below.

2.3 Description of the sFOFO cooling channel

In this subsection, we describe the cooling channel from the perspective of the beam physicist writing the corresponding computer simulation package. Engineering details will be given later.

2.3.1 The lattices

The channel operates at a nominal momentum of 200 MeV/c. There are six sections with steadily decreasing $\beta_{\perp,min}$. In the first three lattices, labeled (1,i), i=1,3, the lattice half period length is 2.75 m, and in the last three lattices, (2,i), i=1,3, this half period length is 1.65 m. The matching sections between these sections also consist of cooling cells, which differ from the regular cooling sections only by the current circulating in the coils, with one exception. A different coil length must be used in the matching section where the lattice period length decreases from 2.75 m to 1.65 m, and the absorber has been removed. The length of these lattices are specified in Table 3.

Specific coil dimensions, current densities are specified on Table 4 . It is assumed that the current density is uniform across the thickness of the coil.

Table 3: Length of the sections and integrated length from the start of the cooling channel.

section	**Length (m.)**	**Total length (m.)**
cool 1,1	$4 \times 2.75 = 11$	11
match 1,1-2	$2 \times 2.75 = 5.5$	16.5
cool 1,2	$4 \times 2.75 = 11$	27.5
match 1,2-3	$2 \times 2.75 = 5.5$	33
cool 1,3	$4 \times 2.75 = 11$	44
match 1,3-2,1	4.4	48.4
cool 2,1	$12 \times 1.65 = 19.8$	68.2
match 2,1-2	$2 \times 1.65 = 3.3$	71.5
cool 2,2	$8 \times 1.65 = 13.2$	84.7
match 2,2-3	$2 \times 1.65 = 3.3$	88
cool 2,3	$12 \times 1.65 = 19.8$	107.8

The design of the matching sections between regular sections with the same lattice cell length goes as follow. In all cases a matching section is inserted and consists of two lattice cells: the first as in the previous cells, the second as in the following cells, except that the currents in the central pair of focus coils are set to an average of the currents in the previous and following focusing coils. For instance, Table 5 describes the match between the (1,1) and (1,2) lattices.

The match where the lattice period changes from 2.75 down to 1.65 m requires further attention. Although the proposed solution is not a perfect match, its mechanical simplicity and relatively short length might actually outweigh the benefit we could get with a slow, adiabatic match from one lattice period to an

Table 4: Geometry and current densities for the solenoids. The first (last) three coil types refer to the 2.75 (1.65) m long cell (half period), respectively. The position refers to the upstream edge of the coil and start from the beginning of half period cell. The radius refers to the inner radius of the coil. Dimension are in m and A/mm^2. The current indices refer to the nomenclature used in the previous table.

Type	**Position**	**Length**	**Radius**	**Thickness**	j(1,1)	j(1,2)	j(1,3)
focusing	0.175	0.167	0.330	0.175	75.20	84.17	91.46
coupling	1.210	0.330	0.770	0.080	98.25	92.42	84.75
focusing	2.408	0.167	0.330	0.175	75.20	84.17	91.46
					j(2,1)	j(2,2)	j(2,3)
focusing	0.066	0.145	0.198	0.330	68.87	75.13	83.48
coupling	0.627	0.396	0.792	0.099	95.65	88.00	76.52
focusing	1.439	0.145	0.198	0.330	68.87	75.13	83.48

other. Note that the absorber in the matching cell is removed, allowing us to run the upstream and downstream linac closer to the bunching condition, giving us a slight increase of the r.f. bucket size, and ease of mechanical assembly. Coils and current are listed on table 6. The magnetic field on axis for the entire cooling channel is shown on figure 7.

2.3.2 Cooling *rf*

The lengths of the linacs are constrained by the lattices themselves, as the focusing coils have a bore radius smaller than the *rf* cavities, and by the *rf* cell length, which must be optimized to give the high Q required to reach high gradient. These linacs are always placed in the middle of the half-period lattice cell. Each cell can be phased separately. In order to improve the Q of the cavity, the iris of the cell must be covered with a foil or a grid.

Our baseline design calls for thin, pre-stressed beryllium windows with thicknesses that increase with radius. This arrangement is justified on two separate grounds. (i) The power dissipated on the iris or foil goes like the 4th power of the radius (at relatively small radius). We therefore need more thickness at higher radius to remove the heat. (ii) The particles at large radius tend to have large transverse amplitude and are "warmer" than the central core. One can therefore afford a bit more multiple scattering at such large radius. Note also that the windows on each end of the linacs dissipate half the power than the windows at the boundary between two adjacent cells. Thus, these edge windows are thinner than those in the center of the linac. The parameters of these linacs are listed on Table 7 and the *rf* window parameters are in Table (REFER TO TABLE 18.D HERE).

The use of thin aluminum tubes arranged in a Cartesian grid can also be

Table 5: Geometry and current densities for the solenoids in the first matching section. Coil locations are given with respect to the start of the channel. Dimension are in m and A/mm^2. The coil dimensions are specified in Table 4.

Type	**Location [m]**	**j(1,i)**
last 1,1		
focusing	11.175	75.20
coupling	12.210	98.25
focusing	13.408	75.20
match		
focusing	13.925	-75.20
coupling	14.960	-98.25
focusing	16.158	-80.07
focusing	16.675	80.07
coupling	17.710	92.42
focusing	18.908	84.17
first 1,2		
focusing	19.425	-84.17
coupling	20.460	-92.42
focusing	21.658	-84.17

considered, as briefly discussed in the engineering section.

2.3.3 The absorbers

The absorber material is liquid hydrogen (LH2). The density is approximately 0.071 g/cm^3. The energy loss, as given by the Bethe-Bloch formula[8] with a mean excitation energy of 21.9 eV, is 4.6 MeV cm^2/g. The length of these absorbers is 35 cm for the (1,i), i=1,3 lattices and 21 cm for the (2,i) lattices, respectively. The muons therefore lose $\approx$ 12 MeV per lattice cell for the (1,i) lattices and $\approx$ 7 MeV for the (2,i) lattices. This includes the energy loss in the windows. The LH2 vessels must also be equipped with thin aluminum windows. Their thickness is 360 μm (220), with a radius of 18 (11) cm, for the (1,i) and (2,i) lattices, respectively.

Table 6: Geometry and current densities for the solenoids in the matching section between the (1,3) and (2,1) lattices. Coil locations are given with respect to the start of the channel. Distances are given in meters.

Type	**Location**	**Length**	**Radius**	**Thickness**	j (A/mm^2)
last 1,3					
focusing	41.425	0.167	0.330	0.175	91.46
coupling	42.460	0.330	0.770	0.080	84.75
focusing	43.658	0.167	0.330	0.175	91.46
match					
focusing	44.175	0.167	0.330	0.175	-91.46
coupling	45.210	0.330	0.770	0.080	-84.75
focusing, match	46.393	0.198	0.330	0.175	-95.24
focusing	46.816	0.145	0.198	0.330	56.39
coupling	47.377	0.396	0.792	0.099	95.65
focusing	48.189	0.145	0.198	0.330	68.87
first 2,1					
focusing	48.466	0.145	0.198	0.330	-68.87
coupling	49.027	0.396	0.792	0.099	-95.65
focusing	49.839	0.145	0.198	0.330	-68.87

Table 7: Geometry and *rf* parameters for the linac in the cooling channel.

Lattice type	**# of cells**	**Cell length (m)**	**Peak Voltage (MV/m)**	**Phase (deg)**
(1,i), i=1,3	4	0.466	15.48	40.
(1,3 match)	4	0.466	15.48	18.8
(2,1 match)	2	0.559	16.72	18.8
(2,i), i=1,3	2	0.559	16.72	40

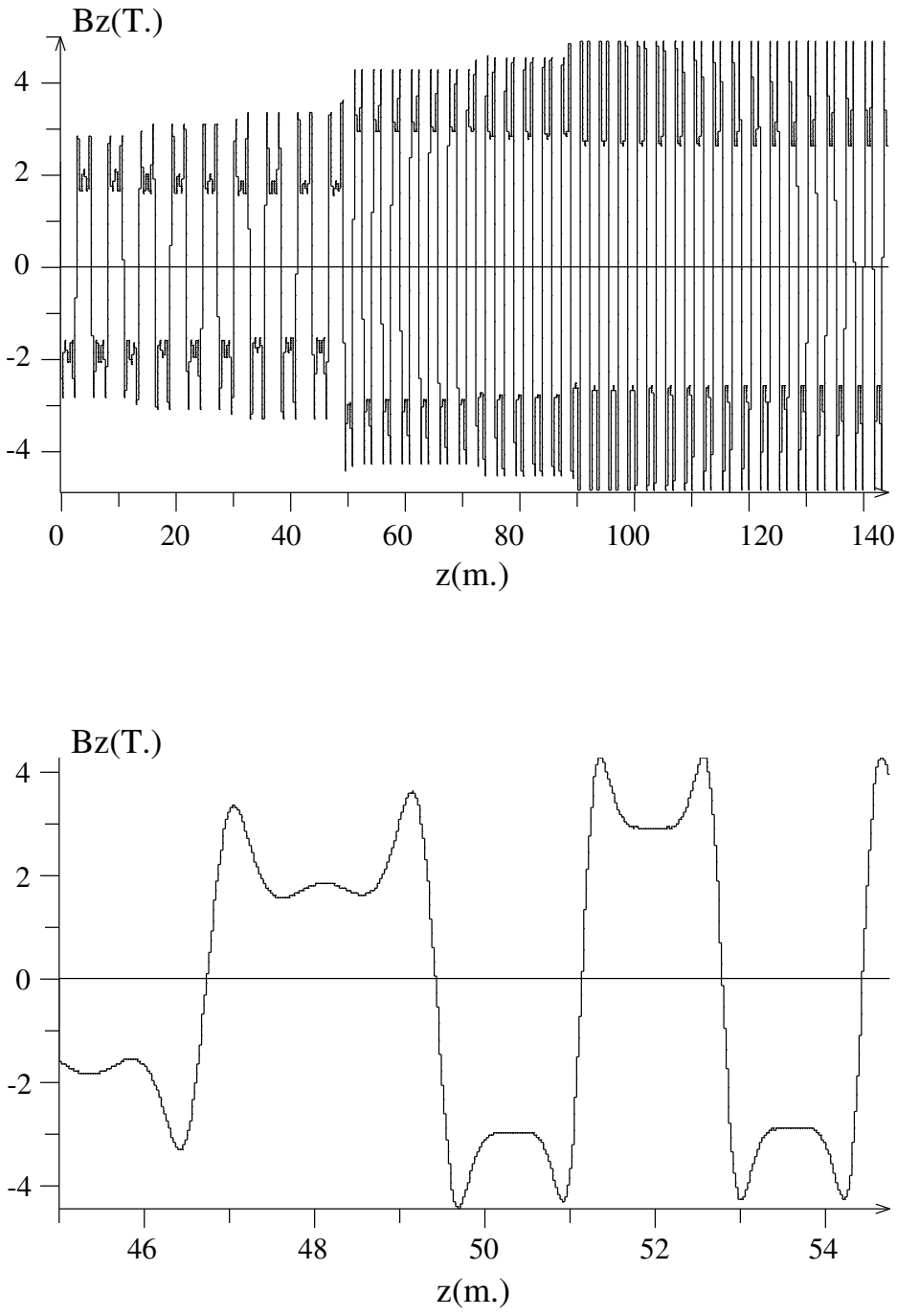

Figure 7: Bz on axis for the entire sFOFO cooling channel (top) and for the matching section between (1,3) - (2,1) lattices.

2.4 Performance

Fig. 8 shows the beta functions and radii, which step down with each new section of the cooling lattice (ICOOL result) . The *rms* angular size is kept substantially constant in order to minimize the effects of multiple scattering. The $\beta_{\perp,min}$ function, derived from the beam second order moments estimated at the absorber's center using Geant4, is shown on Figure 9.

The transverse and longitudinal emittances through the cooling system are shown in Fig. 10. They were obtained based on the ICOOL simulation code and calculated using the code ECALC9 [7]. Emittances are computed in this code using diagonalized covariance matrices. The emittance values are corrected for correlations between the variables, including the strong momentum-transverse amplitude correlation. The transverse and longitudinal emittances obtained in the Geant4 version are shown in Figure 11. At equilibrium a transverse emittance of 2.2 mm rad is reached, consistent with the ICOOL result.

The transverse emittance cools from 12 to 2 mm rad. The longitudinal emittance shows an initial rise as particles not within the *rf* bucket are lost, and then an approach to an asymptotic value set by the bucket size. Naturally, this longitudinal emittance should rise due to straggling and the negative slope of energy loss with energy. However, since the *rf* bucket is already full, instead of an emittance growth we have a steady loss of particles, as seen in Fig. 12.

Despite this overall loss, the numbers of particles within the accelerator acceptance increases. The lower two curves give the number of particles within the baseline longitudinal and transverse acceptances. The middle line represents the values for the accelerator parameters in this study. The lower line, given for comparison, gives the values for the acceptances used in Feasibility Study 1 [1].

- Longitudinal (FS1 & FS2): $(dz^2)/\beta_s \ + \ (dp/p)^2 \ \beta_s \ < \ 150$ (mm)
- Transverse (FS2): $(x^2 + y^2)/\beta_\perp \ + \ (x'^2 + y'^2)\beta_\perp \ < \ 15$ (mm rad)
- Transverse (FS1): $(x^2 + y^2)/\beta_\perp \ + \ (x'^2 + y'^2)\beta_\perp \ < \ 9.75$ (mm rad)

where β_s is the synchrotron beta function ($\beta_s = \sigma_{dz}/\sigma_{dp/p}$), and $\beta_\perp$ is the transverse β function.

It is seen that the gain in muons within the accelerator acceptance due to cooling is 3.1 × (or 5 × if the study 1 acceptances were used). If the particle loss from longitudinal emittance growth could be eliminated, as should be the case if emittance exchange were used, then these gains would double. Similar performance is obtained with the Geant4 code, as shown in Figure 13

The beam characteristics in the buncher and cooler sections are summarized in Table 8. The beam is symmetric in this lattice, so the y properties are similar to those in x. We see that the size steadily decreases as we proceed down the channel. The angular divergence is kept constant for maximum cooling efficiency. The momentum spread of the entire beam is still large after the induction linac, but this includes very low and high energy muons that do not get transmitted through the subsequent sFOFO lattice. The decrease in energy

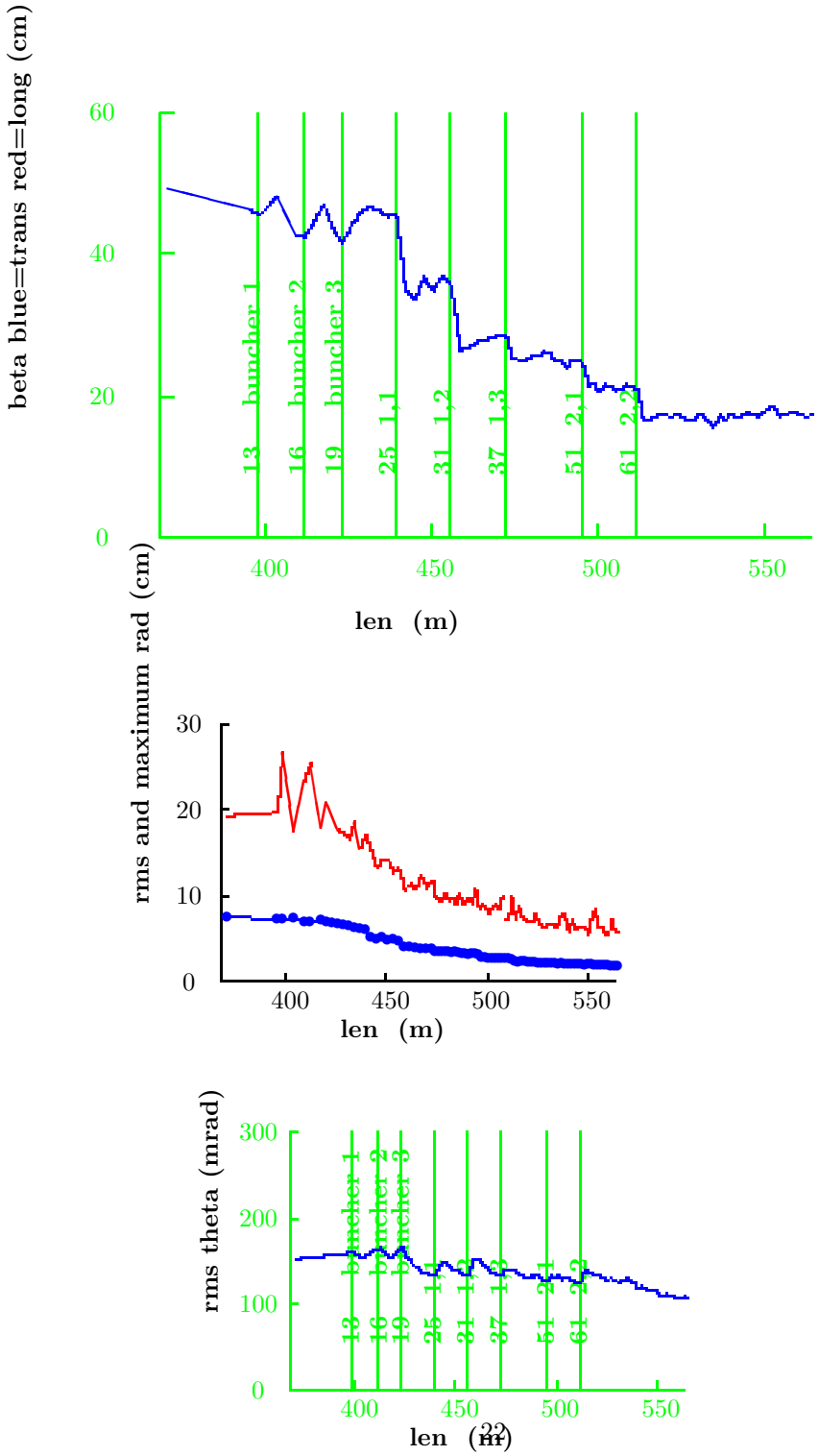

Figure 8: beta function in the buncher and cooling sections; *rms* beam radius; *rms* divergence.

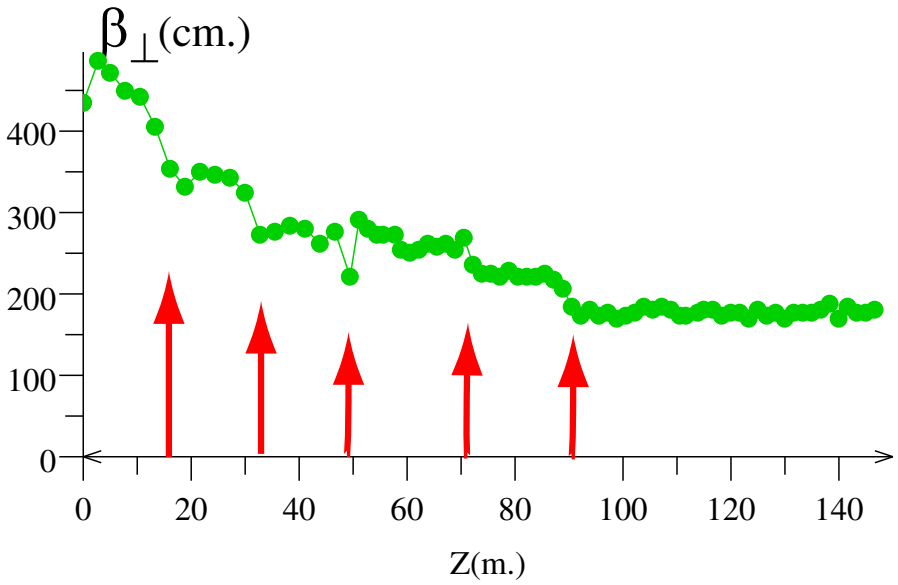

Figure 9: The $\beta_\perp$ function, average over the relevant momentum bite, and measured from the second order moments of the beam itself, as the cooling progresses, for the entire SFOFO cooling channel. The 5 arrows indicate the beginning of the (1,2), (1,3), (2,i), i=1,3 lattice sections

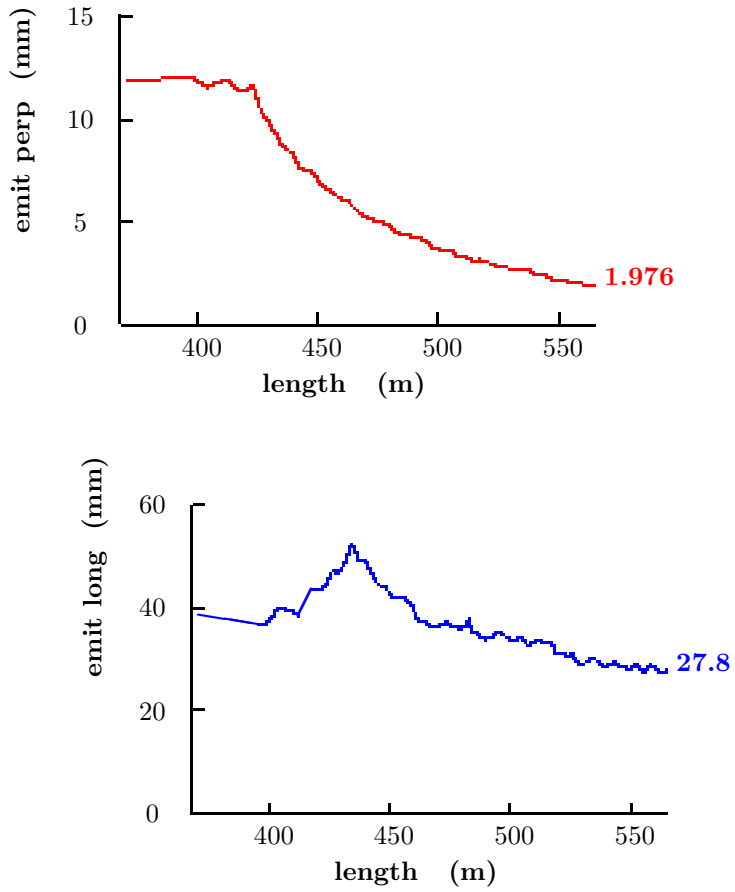

Figure 10: Transverse and longitudinal emittances in the buncher and cooling sections.

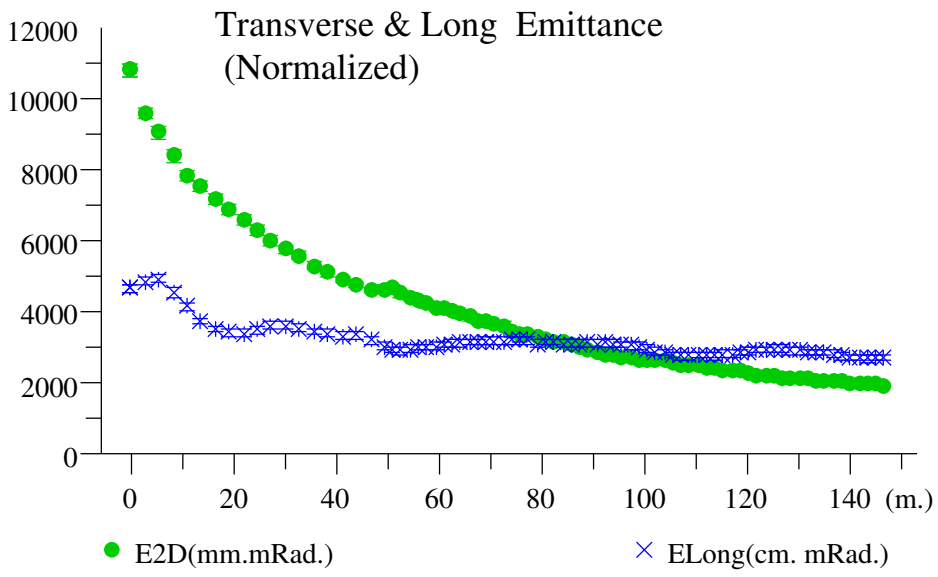

Figure 11: The longitudinal and transverse emittances.

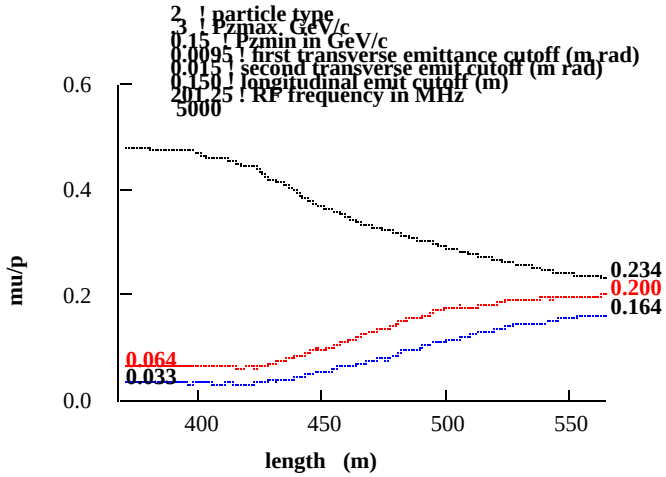

Figure 12: Particle transmission in the buncher and cooling sections; top curve is overall muons per incident proton; middle curve is acceptance into 15 mm transverse acceptance; lower curve is acceptance into 9.5 mm transverse acceptance.

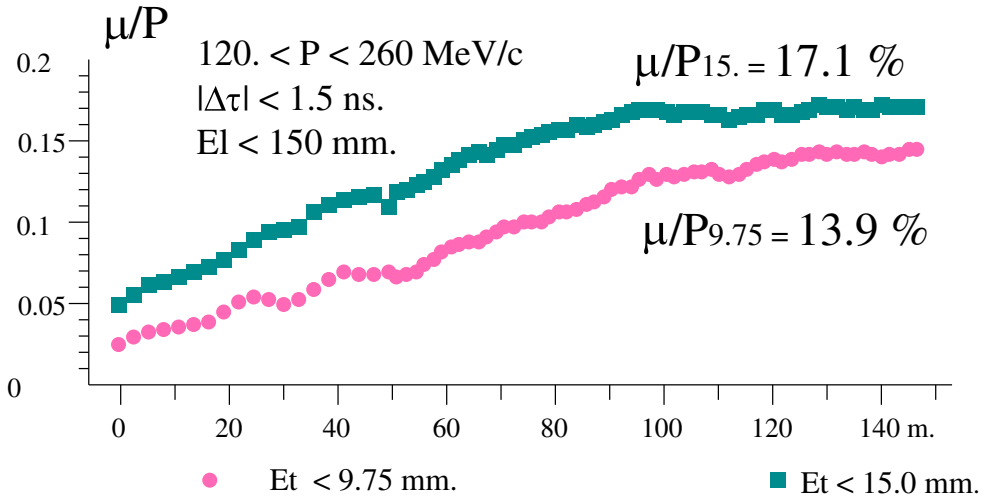

Figure 13: The muon to proton yield ratio for the two transverse emittance cuts, clearly showing that the channel cools as the density in the center of the phase space increases.

spread is due to particle losses since there is no longitudinal cooling or emittance exchange in this lattice. Likewise, the average momentum of the beam decreases until it matches the acceptance of the sFOFO lattice. The time spread refers to a single bunch in the bunch train.

The longitudinal emittance remains more or less stable, at around 30 mm. This is in part deceptive. Straggling and imperfections in the longitudinal to transverse correlation[1] cause particles to fall out of the *rf* bucket and to be scraped away due to the strong π betatron resonances. In fact, the buncher delivers a full *rf* bucket to the cooling section and the longitudinal emittance cannot grow any larger. This scraping occurs on the combined time scale of

[1] described in the bunching section

Table 8: Beam characteristics summary

location (end of)	σ_x cm	$\sigma_{x'}$ mrad	σ_p MeV/c	σ_t ns	$\langle p \rangle$ MeV/c
induction linac	8.6	95	113		260
matching section	5.8	114	113		260
buncher	5.3	107	111	0.84	256
2.75 m cooler	3.0	91	70	0.55	226
1.65 m cooler	1.8	102	30	0.51	207

a synchrotron period, about 20 m, and on the growth time of the betatron resonance instability.

The performance of the cooling channel is limited by both multiple scattering and the limited momentum acceptance. While the latter is difficult to estimate based on computer simulations, it is straightforward to estimate the former contribution by simply turining off multiple scattering in the code. If so, the relative μ/P_{15} and $\mu/P_{9.75}$ yields would increase by 11 % and 19 %, respectively.

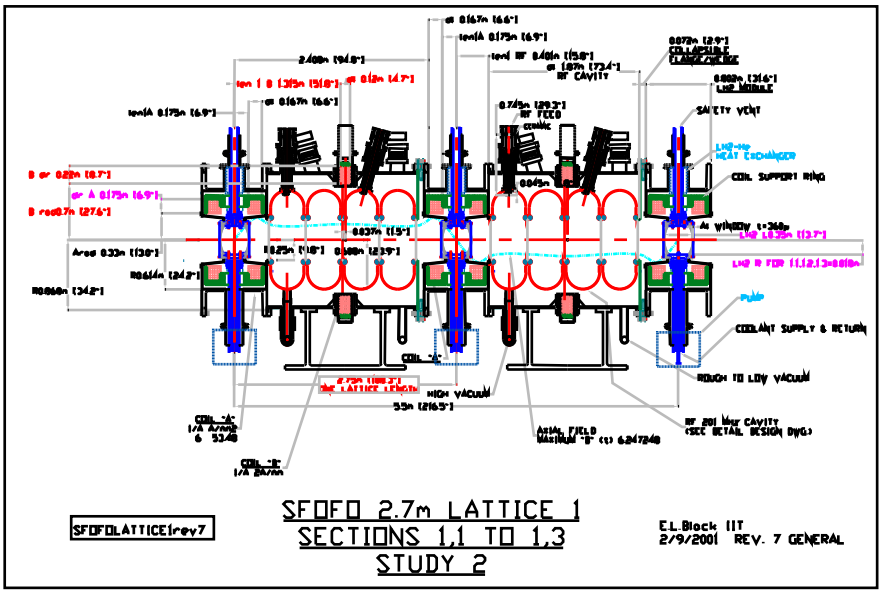

Figure 14: Engineering detail of the 2.75 m cooling lattice cell.

2.5 Engineering details

DESCIPTIVE TEXT IS NEEDED HERE

A detailed layout of a 2.75 m lattice cell is shown in Fig. 14.

A detailed layout of a 1.65 m lattice cell is shown in Fig. 15.

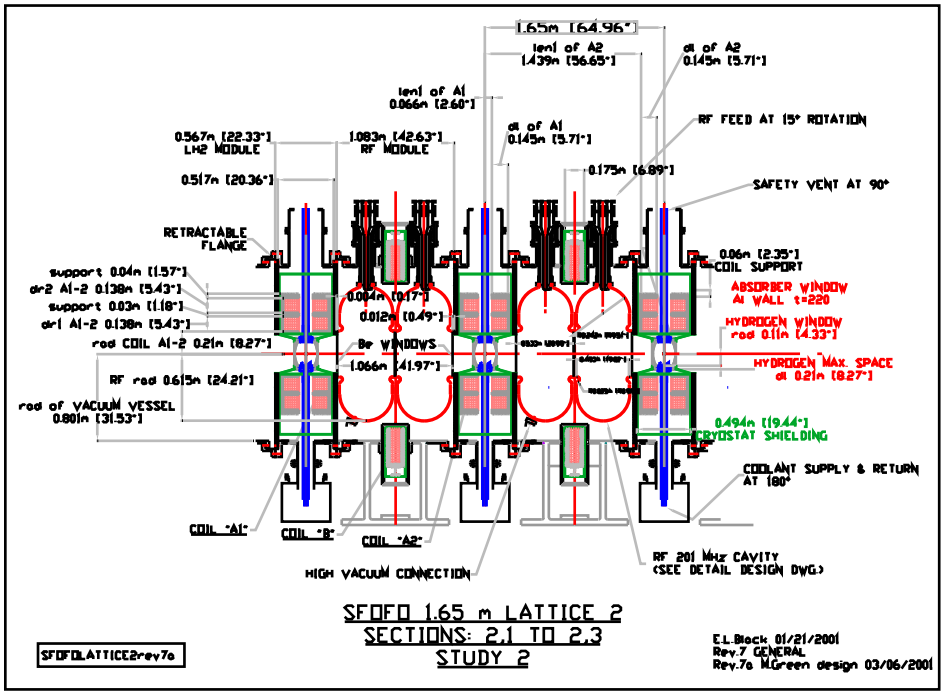

Figure 15: Engineering detail of the 1.65 m cooling lattice cell.

2.6 *rf* systems

The *rf* systems for the buncher and the cooler are required to match the muon beam into the longitudinal acceptance of the cooling channel and replenish the beam energy lost during ionization cooling. Since they must operate inside the strong solenoid fields, they cannot be superconducting. These systems require a large number of *rf* cavities operating at high gradient, and a large amount of pulsed *rf* power. They are technically challenging and expensive and have therefore been the focus of continued development during study II. The cooling channel layout has continued to evolve since study I with emphasis on integration of realistic components into the available space along with optimization of the channel performance. The buncher and cooling channel systems must accommodate liquid hydrogen absorbers, high gradient *rf* cavities, windows, tuners, superconducting solenoids, diagnostics, pumping, harmonic cavities and other equipment. The system must be designed in such a way as to allow assembly and access for maintenance.

The buncher and cooling channel will be made of a large number of modules. Each module contains two or four 201.25 MHz closed-cell cavities and is powered by one or two high power klystrons. The density of equipment in the building is therefore high and the systems must be carefully laid out to allow access for installation and maintenance.

The proposed buncher and cooling channel is approximately 163 m long and requires 162 cavities and 73 klystrons. The total installed power is approximately 690 MW. (REFER TO SECTION 18 FOR DETAILS)

2.6.1 Power sources

The ionization cooling channel requires high peak *rf* power sources at 201.25 MHz and 402.5 MHz to efficiently cool the muon beam. There are 162, 201.25 MHz cavities in the channel that require 687 MW of *rf* power for a pulse length of 115 ms at 15 Hz and 6, 402.5 MHz cavities that require 1.8 MW at 15 Hz. An examination of the requirements shows that an *rf* source of about 5 to 12 MW would be ideal for the 201.25 MHz cavities and a source of 500 to 750 kW for the 402.5 MHz cavities.

The *rf* for the 201.25 MHz cavities could be supplied by existing gridded tubes at about the 5 MW level. However, the low gain and lifetime of gridded tubes make the R&D effort to develop an alternative most attractive. Preliminary calculations at SLAC have shown that a 201.25 MHz klystron could be built with a reasonable amount of R&D. SLAC has examined two designs: a single gun diode design, and the multibeam klystron. The multibeam klystron is the most attractive in that it reduces the overall length of the tube from 7.5 m to between 3.5 and 4.0 m. The length reduction factor of the multibeam klystron and its potential for higher efficiency make it the optimum candidate for the neutrino factory. The length of the multibeam klystron is, also, consistent with the manufacturing capabilities of current tube manufacturers. However the manufacture of a 7.5 m diode tube would be a big step and would require

new and costly facility upgrades. To provide *rf* power overhead for dynamic regulation of the *rf* phase and amplitude, a 12 MW multibeam klystron has been selected as the high power *rf* source for the neutrino factory. This provides an *rf* power overhead margin of about 20 % for regulation.

The 12 MW multibeam klystron design should be a fully integrated horizontal package incorporating the tube, solenoid, and high voltage terminal, as pioneered at CERN for LEP. This would facilitate the replacement and installation of tubes in the facility. Another advantage, besides the ease of handling, is the reduced cost of the *rf* building because of the lower building height requirement. The transmission lines from the tubes to the cavities will be large coaxial lines because of the large size and costs of waveguide . Power splitters would divide the *rf* power from each tube to supply the appropriate *rf* power to the cavities. Splitters with proper built in phase delays would divide the power to each cell or cavity section of the cooling channel. (REFER TO SECTION 18 FOR DETAILS)

2.6.2 Cavities

The 201.25 MHz normal-conducting cavities in the cooling sections must operate at very high accelerating gradients. This would be impractical with conventional open iris structures because of the large size of the beam iris required. A great improvement can be made in the shunt impedance of the cavity by closing the iris with a thin conducting barrier. This barrier must use the smallest amount of material to minimize scattering of the muon beam. It is proposed to close the irises with thin beryllium foils. Other methods of closure, such as grids of thin-walled tubes, will be evaluated in the future. The foils must be thick enough to conduct away the heat from the *rf* currents and keep the temperature to a predetermined level. The foils will be pre-stressed in tension during manufacture in order to keep them flat. This method had been tested experimentally and works well up to the point where the thermal expansion exceeds the pre-stress and the foils begin to move. Foil thicknesses have been chosen for study II which should keep the temperatures below this critical level. The use of tapered foils or foils with stepped thickness can reduce the amount of material intercepted by the core of the beam, reducing the amount of scattering significantly.

The normal-conducting cavities in the buncher can be of the same design as those in the first cooling section, except that they would be operated at lower gradient. This will allow the use of thinner foils to minimize the scattering. The buncher section also contains a small number of harmonic cavities operating at 402.5 MHz. These fit into the spaces normally occupied by the hydrogen absorbers in the cooling cells. For these cavities the foils occupy most of the diameter of the end walls, but the gradients are much lower, so the losses in the foils are manageable.

The normal conducting cells must have some cooling to remove the average power losses in the walls and to stabilize the frequency. The study II design has been evaluated for room temperature operation although the option of operating at reduced temperature has been kept open. This would lower the wall resistance

and reduce the peak power requirements at the expense of adding a potentially large refrigeration system. (REFER TO SECTION 18 FOR DETAILS)

2.7 Superconducting Solenoids for the Muon Cooling Cells

2.7.1 Layout and parameters

The matching section consists of two 2.75-meter long cells and about 2.5 meters of solenoids that have a warm bore diameter of 600 mm. These solenoids must be designed to withstand longitudinal forces of up to 60 metric tons that are imparted on them by the two matching cells downstream. The solenoids in the matching section cells are the same as in the cells in the beam bunching section. The twenty 2.75-meter long bunching cells are the same as the 2.75-meter long cooling cells. The warm bore aperture of the of the A coils for a 2.75-meter long cooling cell must be about 650 mm in order to accommodate a liquid hydrogen absorber (See Figure 16. The A coils described in this section were refered to as focusing coils earlier. The B coils desribed here were refered to as coupling coils). The warm bore aperture for the beam bunching cell flux reversal coils must be the same in order to accommodate a 402.5 MHz *rf* cavity. Room temperature service ports to the 402.5 MHz *rf* cavity can go out through the flux reversal magnet cryostat between the flux reversal coils. Table 9 shows the number of cells of each type, the minimum aperture requirements for the magnets and the maximum coil current densities for the coils in each cell type. Included in Table 9 is the magnetic field 9.9 meters from the beam axis. Because the bunching and cooling cell solenoids are constantly changing polarity, there is almost no stray field from these solenoids at R = 10 meters.

Table 9: Basic cell parameters for the beam bunching and cooling cell

Parameter	2.75 m Cell	1.65 m Cell
Number of Cells of This Type	39	37
Cell Length (mm)	2750	1650
Maximum Space for the *rf* Cavity	1966	1108
Number of 201.25 MHz *rf* Cavities per Cell	4	2
Number of 402,5 MHz *rf* Cavities per Bunching Cell	1	NA
A Magnet Cryostat Length (mm)	784	542
B Magnet Cryostat Length (mm)	283	209
Aperture for the A Magnet (mm)	650	370
Aperture for the B Magnet (mm)	1390	1334
Maximum A Coil Current Density (A mm^{-2})	128.04	99.65
Maximum B Coil Current Density (A mm^{-2})	99.24	109.45
Maximum Cell Stored Energy (MJ)	13.2	17.6
Maximum Longitudinal Warm to Cold Force (MN)	0.74	1.20
Number of Longitudinal Supports per Coil	4	6 to 8
Peak Induction 9.9 m from the Cell axis (T)	$1.18x10^{-5}$	$2.62x10^{-5}$

Magnet parameters and a magnet cross-section for the 2.75-meter long bunching and cooling cell magnets are shown in Table 10 and Figure 16. Note: the solenoids in the 2.75-meter long cells are the same for both bunching and cooling cells. Magnet parameters and a magnet cross-section for the 1.65-meter long

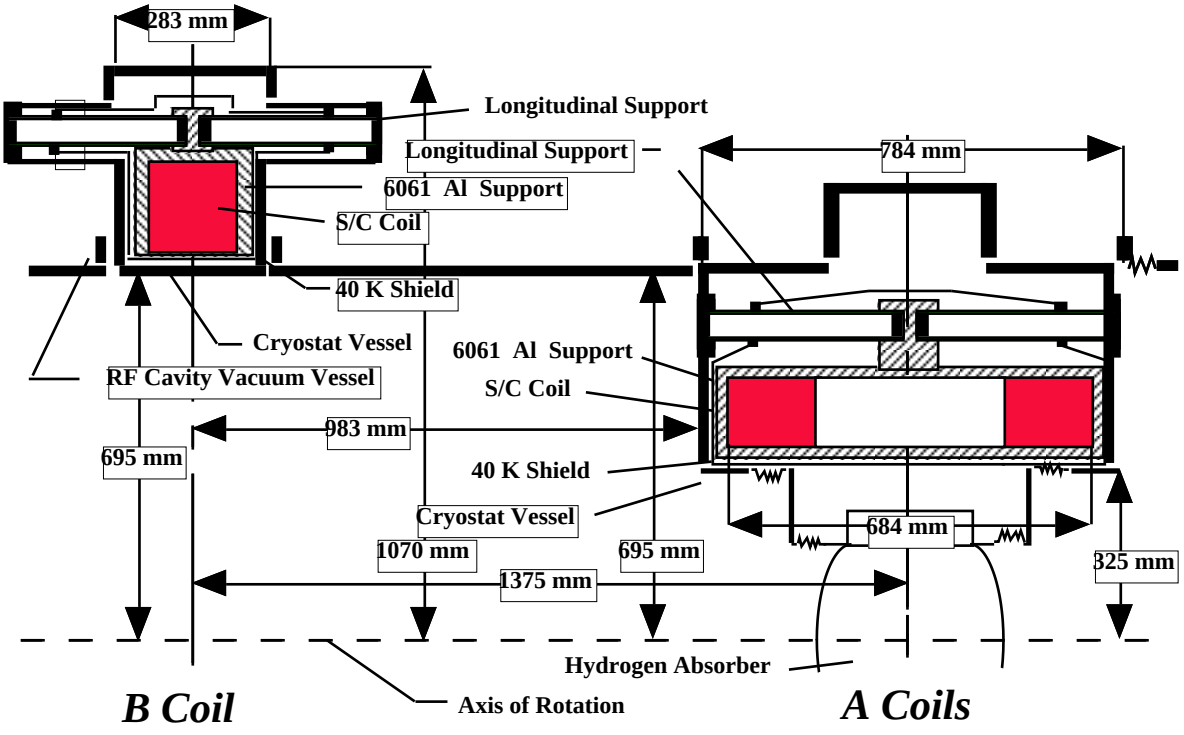

Figure 16: Magnet Cross-section for the 2.75-meter Long Cooling Cell.

Figure 17: Magnet Cross-section for the 1.65-meter Long Cooling Cell.

cooling cell magnets are shown in Table 11 and Figure 17. The solenoid magnet cross-sections shown in Figures 17 and 18 are through the longitudinal supports. The penetration of the hydrogen absorber plumbing through the space between the A coils is not shown in Figures 16 and 17.

Table 10: Solenoid parameters for the 2.75-meter long bunching and cooling cell

	A Magnets	B Magnets
Physical Parameters		
Magnet Cryostat Length (mm)	784	283
Magnet Cryostat Bore Diameter (mm)	650	1390
S/C Coil Length (mm)	167	162
Inner Radius of the Coil (mm)	355	729
S/C Coil Thickness (mm)	125	162
Distance Between Coils in Z Direction (mm)	350	NA
Inner Support Structure Thickness (mm)	15	0
Outer Support Structure Thickness (mm)	20	25
Number of Turns per Magnet	2304	1472
Magnet Cold Mass (kg)	1430	1245
Magnet Overall Mass (kg)	1870	1570
Electrical Parameters and Magnetic Forces		
Maximum Magnet Design Current (A)	2320.2	1779.9
Peak Induction in the Windings (T)	7.5	6.5
Magnet Stored Energy at Design Current (MJ)	≈7.9	≈7.7
Magnet Self Inductance per Cell (H)	≈2.9	≈4.9
Superconductor Matrix J (A mm^{-2})	155	119
E J2 Limit per Magnet Cell (J A^2 m^{-4})	$1.89x10^{23}$	$1.09x10^{23}$
Force Pushing the A Coils Apart (metric tons)	329	NA
Peak Fault Force on a the Coil (metric tons)	75.3	75.3

Figures 16 and 17 show a cross-section of the bunching and cooling cell solenoids. The plane for the cross-sections is taken through the warm to cold supports that carry axial forces. The cross-sections in Figures 16 and 17 show the magnet cryostats, the coils, the coil support structure, the 30 K shields, and the vacuum vessel around the *rf* cavities. The cryostat vacuum systems are separated from the vacuum around the *rf* cavities and the beam vacuum.

Figure 18 shows a cross-section through the center of the 1.65-meter long cell A coil pair. Note the location of the longitudinal cold mass supports and the cold mass supports that carry forces in both directions perpendicular to the solenoid axis. The figure illustrates how magnet electrical leads, and helium refrigeration can be brought into the cryostat. Figure 18 is a typical cross-section that can

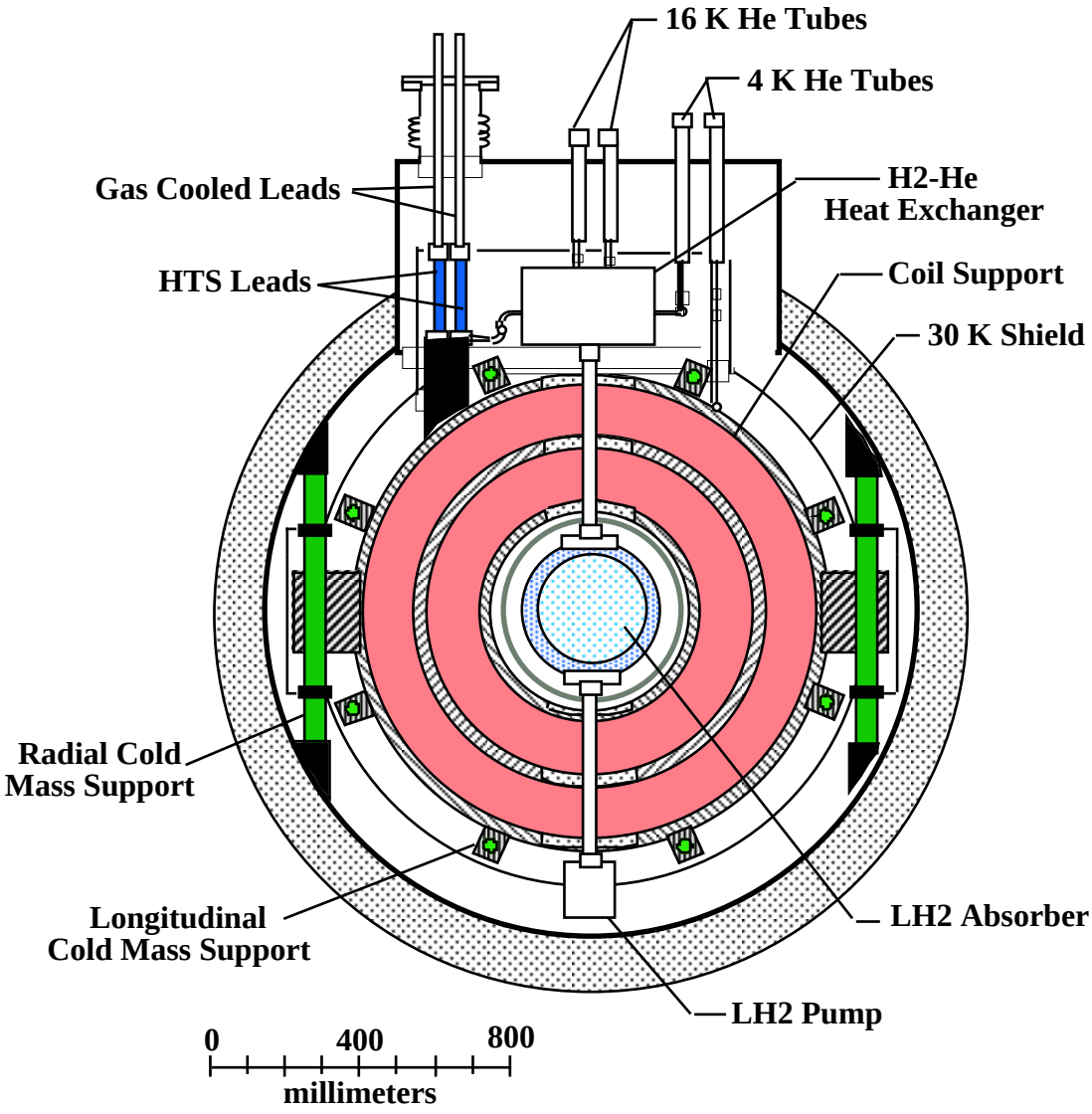

Figure 18: Cross-section of the 1.65 m Cell A Magnet Perpendicular to the Beam.

Table 11: Solenoid parameters for the 1.65-meter long cooling cell

	A Magnets	B Magnets
Physical Parameters		
Magnet Cryostat Length (mm)	542	209
Magnet Cryostat Warm Bore Diameter (mm)	380	1334
S/C Coil Length (mm)	145	109
Inner Radius of Inner Coil	210	687
S/C Coil Thickness (mm)	138	326
Distance Between Coils in Z Direction (mm)	132	NA
Inner Support Structure Thickness (mm)	20	0
Center Support Structure Thickness (mm)	30	NA
Outer Support Structure Thickness (mm)	40	25
Number of Turns per Magnet	4480	1974
Magnet Cold Mass (kg)	1995	1750
Magnet Overall Mass (kg)	2430	2290
Electrical Parameters and Magnetic Forces		
Maximum Magnet Design Current (A)	1780.5	1896.7
Peak Induction in the Windings (T)	8.4	6.5
Magnet Stored Energy at Design Current (MJ)	≈10.7	≈11.0
Magnet Self Inductance per Cell (H)	≈6.8	≈6.1
Superconductor Matrix J (A mm^{-2})	119	126
E J2 Limit per Magnet Cell (J A^2 m^{-4})	$1.51x10^{23}$	$1.74x10^{23}$
Force Pushing the A Coils Apart (metric tons)	1980	NA
Peak Fault Force on a the Coil (metric tons)	122	122

be applied to all of the bunching and cooling cell solenoids.

Figures 16 and 17 show the location of the hydrogen absorbers within the bore of the A coil pair. The hydrogen absorber will share the same cryostat with the A coils. The hydrogen absorber and the A magnet will have a common vacuum and the hydrogen absorber will be supported from the A coil package by a low thermal conductivity support system made from a titanium tube. Figure 18 illustrates schematically that connections to the hydrogen absorber can be made between the A coils through the support structure that carries the magnetic large forces generated by the two A coils that operate at opposing polarities.

2.7.2 Forces

Forces in the longitudinal direction are a serious concern for the bunching and cooling solenoids. The field flip coils (the A coils) generate large forces (up to 1950 metric tons) pushing them apart. These forces must be carried by a 4.4 K metallic structure between the two coils. The magnitude of the forces pushing the A coils apart depends on the spacing between the coils, the average coil diameter and the current carried in each coil. The inter-coil forces are carried

by either aluminum of stainless steel shells on the inside and the outside of the coils. The forces are transmitted to the coil end plates, which are put in bending. Large stresses are developed at the point where the end plates meet the shells inside and outside the coils. Since the force between the A coils in the 1.65-meter long cooling cells is so large (about 1950 metric tons), the A coils had to be divided in the radial direction in order to reduce the bending stress in the end plates. The large stress in the end plates of the A coils in the 1.65-meter long cooling cell dictate that the end plates and shells around the A coils must be made from 316 stainless steel.

If the currents in all of the A coils and all of the B coils were the same from cooling cell to cooling cell, there would be no net longitudinal force on any of the coils. The currents in the cooling cell coils vary as one goes down the bunching and cooling channel. This generates a longitudinal force in various magnet coils. The largest longitudinal forces will be generated at the ends of the string or when one coil quenches and adjacent coils do not quench. One can attach all of the coils together with cold members, but further examination suggests that this approach does not make sense if one wants to be able to assemble and disassemble the muon cooling system. As a result, every magnet is assumed to have cold to warm longitudinal supports. The cold to warm supports in the magnets in the 2.75-meter long cells are designed to carry 80 metric tons (the maximum force during a magnet fault). These forces can be carried by four oriented glass fiber epoxy cylindrical supports that are 50-mm in diameter with a 4-mm thick wall. Oriented glass fiber rods can carry stresses up to 600 MPa in either tension or compression.

The 1.65-meter long cell magnets have longitudinal cold to warm supports that are designed to carry 120 metric tons. Figure 18 shows the location of eight of these supports on the 1.65-meter long cell A magnet. A six support longitudinal support system would also be practical. The support shown for the A coil in Figure 17 is designed to operate in both tension and compression. Further engineering can define an optimum cold mass support system for these magnets. Compared to other heat loads into the magnets, the longitudinal cold mass supports represent about one quarter of the total heat leak into the magnet cryostat.

2.7.3 Conductor

The magnet conductor that is assumed for the all of the B solenoids is a conductor that is 7 parts copper and 1 part niobium-titanium. This conductor consists of strands with a copper to superconductor ratio of 1 to 1.3. The twist pitch in the superconductor is about 10 mm. The strands of this conductor are attached to a pure copper matrix. The overall dimensions for the finished conductor is 3 mm by 5 mm. The proposed conductor will carry 5100 A at 5 T and 4.2 K. At 7.5 T the proposed conductor will carry about 2500 A at 4.4 K. This conductor could be used in the 2.75-meter cell A coils, but the margin is rather tight. The problem occurs in the 1.65-meter long cell A magnet where the peak field at the high field point in the magnet is 8.4 T. This coil must be operated

at reduced temperature (say 2.5 K) when the proposed conductor is used. A re-optimization of the short cooling cell that moves the A coils further apart may be a better solution to the high field problem in the short cell A coils. It is proposed that the A coils in the both types of cells use a conductor with a 4 to 1 copper to superconductor ratio.

The conductor is assumed to have a varnish insulation that is 0.05 mm thick. The layer to layer fiber glass epoxy insulation is assumed to be 0.4 mm thick. The ground plane insulation around the coils is assumed to be 1.6 mm thick. This permits the superconducting coils to be discharged with a voltage across the leads of up to 1200 volts. Each A coil set and each B coil is assumed to be powered separately. A quench protection voltage of 1200 V is adequate to protect any of the coils in the cooling cells. Because the conductor current density is high, the A coils in the 2.75-meter long cells have the smallest safety margin when it comes to quench protection. Re-optimization of these coils can improve their quench protection.

The conductor current and current density given for the A and B coils in Tables 10 and 11 are the peak values that would occur in the cells operating at the highest current. The estimated stored energy occurs at the peak design current in the coils. In general, when the current density is high in the A coil, the current density in the B coil is low. The stored energy for the cooling cells changes very little as one moves down the cooling channel. The cell stored-energy shown in Table 9 is the average stored energy for that type of cell. Table 12 shows the average coil current density and coil current for the A and B coils in the various regions of the bunching and cooling channel.

Table 12: Coil average J and I for various sections of the bunching and cooling channel

Section	No. Cells	A Coil J A mm^{-2}	A Coil I A	B Coil J A mm^{-2}	B Coil I A
Bunching Cells	22	106.34	1927.0	99.24	1779.9
Cooling 1-1	5	106.34	1927.0	99.24	1779.9
Cooling 1-2	6	117.83	2135.3	92.42	1657.8
Cooling 1-3	6	128.04	2320.2	84.75	1520.0
Cooling 2-1	14	82.21	1468.8	109.45	1896.7
Cooling 2-2	10	89.68	1602.3	101.93	1766.4
Cooling 2-3	13	99.65	1780.5	93.47	1619.8

Figure 19 is a schematic representation of the matching section of a 2.75-meter long cell to a 1.65-meter long cell. The forces between the coils in the A magnet are quite large. It is assumed that the structure around the A coils is stainless steel. The A coil set shown in Figure 19 is the only unique magnet is the muon cooling channel. There are 39 A and B coils that make up the 2.75-meter long bunching and cooling cells. There are 37 A and B coils that make up the 1.65-meter long cooling cells.

The last two meters of the induction linac channel must have thicker coils

Figure 19: Cross-section of the Matching Region between 2.75 m Cells and 1.65 m Cells.

Figure 20: Cryogenic Cooling System within a Typical Cooling A Coil Cryostat

with a separate power supply on each coil. The 1.25 T solenoids at the end of the induction cells must have separate longitudinal warm to cold supports to carry forces (up to 60 metric tons) generated by the magnets in the first cells of the bunching section.

2.7.4 Refrigeration

Refrigeration to the muon cooling magnets and hydrogen absorbers is supplied at 16 K and 4.4 K. The 4.4 K refrigeration is used to cool the superconducting coils except for coil A in the 1.65-meter long cell, which is cooled to 2.5 K. The 2.5 K cooling requires an additional heat exchanger and a vacuum pump to produce nearly 0.3 W of cooling at 2.5 K. Most of the heat into the 1.65-meter cell A coil package is intercepted at 4.4 K. The hydrogen absorbers are cooled from the same refrigerator as the solenoid magnets. Refrigeration for the hydrogen absorbers is drawn off at 16 K. The 16 K helium used to cool the liquid hydrogen returns to the helium cold box at 19 K. The absorbers in the 2.75-meter long cell contain 9 liters of liquid hydrogen. The 1.65-meter long cell absorbers contain about 4 liters of liquid hydrogen. The estimated heat load to the absorbers is between 120 and 130 W. Table 13 shows the refrigeration requirements for the 2.75-meter long cells and the 1.65-meter long cells with hydrogen absorbers. The equivalent 4.4 K refrigeration reflects the Carnot ratios from 4.4 K to 16 K and the refrigeration lost when helium returns to the compressor by bypassing the refrigerator heat exchangers. The equivalent 4.4 K refrigeration for each of the 22 bunching cells is 21.1 W per cell. About 10.4 W of equivalent 4.4 K refrigeration is used to cool two pairs of 2000 A gas-cooled leads from 40 K to 300 K.

Figure 20 shows a schematic representation of the refrigeration for a pair of A coils with a hydrogen absorber. Two-phase helium at 4.4 K is used to cool the superconducting coils. If nineteen magnets are cooled from a single flow circuit, the mass flow of two-phase helium should be 8 to 10 grams per second. The flow circuit can have up to 20 magnet coils in series before the helium is returned to the control cryostat. The shields, intercepts, current leads, and hydrogen absorbers are cooled by helium that comes from the refrigerator at 16 K. The helium used to cool the shields and the leads is returned to the refrigerator compress warm. The rest of the 16 K helium returns to the refrigerator at 19 K.

The helium used to cool the magnet shield intercepts heat from the cold mass support, the bayonet tubes, the instrumentation wires and radiation heating through the multi-layer insulation before it is used to cool the gas cooled current leads for the A and B magnet. For the flow circuit shown in Figure 20, the flow of helium gas in the shield cooling circuit is dictated by the needs of the gas cooled current-leads. For the current leads in the cooling and bunching magnets this flow varies from 0.15 to 0.23 grams per second. Depending on the needs of the current leads, the temperature rise in the shield gas flow circuit will vary from 14 K to 23 K. If one could optimize the magnets, the lead current might be as low as 1200 A. With 1200 A current leads the temperature at the top of the high Tc superconducting leads would be about 50 K. It is proposed that both the A and the B magnet shields be cooled using the same 16 K source of gas from the helium refrigerator, but this is not optimum from the standpoint of overall refrigeration system efficiency. When the helium refrigerator cools both the hydrogen absorber and the magnets, there will be enough excess refrigeration capacity available to cool down the magnet coils down in a reasonable time.

The flow in the 16 K circuit to the hydrogen absorber is dictated by the heat load in the absorber. Without a muon beam, the heat load could be as low as 22 W. With beam heating and the circulation heater operating the heat load into the absorbers can approach 130 W. The temperature rise in the absorber cooling helium circuit should be limited to about 2 K. As a result, the helium flow circuit used to cool the hydrogen absorbers should be designed to provide 12.5 grams per second of 16 K helium. This gas will be returned to the refrigerator cold box at around 19 K (including heating in the return transfer line).

2.7.5 Quench protection

The bunching section has twenty magnets and twenty-one B magnets that have the same current in the coils. The number of cooling section cells where magnets carry the same current is up to thirteen. It is assumed that each magnet in the bunching and cooling sections has its own leads. The magnets can be powered individually or in strings of magnets that carry the same current. Powering magnets as a string of magnets requires a more complicated quench protection system that uses diodes and resistors to cause the string current to by-pass the quenching magnet. For simplicity sake, it is assumed that each magnet has its own power supply and quench protection system. A 2500 A power supply for charging and discharging a single magnet coil (either an A coil or a B coil) should be capable of developing 7 volts. The magnet quench protection consists of a dump resistor across the magnet leads. When a quench is detected, a fast switch disconnects the power supply from the magnet. In all cases, the power supply control system should permit one to control the current and the voltage across the coils as the magnet is charged and discharged. The power supply is not required to operate at both positive and negative currents. A controller is used to control the charging and discharging voltages across each coil and regulate the current once the coil has reached its set current.

2.7.6 Alignment

The B coils can be aligned so that the solenoid axis is correct to 0.3 m-radians. The magnetic center of the B coil can be maintained to about 0.3 mm. The alignment of the A coils can probably be maintained to about 0.5 or 0.6 m-radians. Correction dipoles can be installed in the bore of the A coils that will permit the apparent solenoid axis to be corrected by $\pm$ 1.5 m-radians.

Table 13: Sources of heat at 4.4 K, 20 K and 35 K in the bunching and cooling cell magnets

Source of Heat	2.75 m Cell(W)		1.65 m Cell(W)	
	A Coil	B Coil	A Coil	B Coil
Magnet Heat Loads at 4.4 K				
Vertical Cold Mass Supports	0.24	0.24	0.40	0.24
Longitudinal Cold Mass Supports	0.36	0.36	0.74	0.54
Thermal Radiation through MLI	0.16	0.14	0.01	0.19
Bayonet Joints and Piping	0.03	0.03	0.03	0.03
Instrumentation Wires	0.02	0.02	0.02	0.02
HTS Current Leads	0.60	0.60	0.60	0.60
Total 4.4 K Heat Load per Coil	1.41	1.39	1.80	1.62
Magnet Heat Loads at 2.5 K				
Vertical Cold Mass Supports	—	—	0.05	—
Longitudinal Cold Mass Supports	—	—	0.10	—
Thermal Radiation through MLI	—	—	0.11	—
Bayonet Joints and Piping	—	—	0.01	—
Instrumentation Wires	—	—	0.00	—
HTS Current Leads	—	—	0.02	—
Total 2.5 K Heat Load per Coil	0.0	0.0	0.29	0.0
Magnet Shield and Intercept Heat Loads at 16 to 40 K				
Vertical Cold Mass Supports	3.8	3.8	3.8	3.8
Longitudinal Cold Mass Supports	7.2	7.2	10.8	10.8
Thermal Radiation through MLI	2.7	2.9	1.9	3.2
Bayonet Joints and Piping	1.3	1.3	1.3	1.3
Instrumentation Wires	0.1	0.1	0.1	0.1
Gas Cooled Current Leads	—	—	—	—
Total 16 to 40 K Heat Load per Coil	15.1	15.3	17.9	19.2
Hydrogen Absorber (16 K Cooling)				
Cold Mass Supports	1.5	—	1.0	—
Thermal Radiation through MLI	0.3	—	0.2	—
Bayonet Joints and Piping	1.3	—	1.3	—
Instrumentation Wires	0.1	—	0.1	—
Thermal Radiation to Windows($\epsilon = 0.2$)	18.4	—	6.9	—
Beam Absorption Heating	77.0	—	81.0	—
Circulation Heater	≈30	—	≈30	—
Total 16 K Heat Load per Coil	128.6	0.0	121.5	0.0
Equivalent 4.4 K Refrigeration per Cell	54.6		57.6	

2.8 Liquid hydrogen absorbers

2.8.1 Power handling

We estimate the maximum power dissipation per absorber to be about 300 W, dominated by the ionization energy loss of the muons. The main technical challenge in the absorber design is to prevent boiling of the hydrogen near the beam axis, where the power density is greatest. This requires that the hydrogen flow have a significant component transverse to the beam. We are investigating two ways to achieve this: a design in which the absorber connects to an external heat-exchange and temperature-control loop, and a design in which the absorber vessel is itself the heat exchanger, and heat transfer within the absorber is accomplished dominantly by convection.

The flow-through design resembles previous high-power liquid-hydrogen targets [18, 19], which have been operated successfully at power dissipations as high as 200 W [19] and proposed for operation at dissipations in excess of 500 W [20, 22]. In this aproach the hydrogen is pumped around a loop that includes the absorber vessel as well as a heat exchanger and a heater. In the heat exchanger, which runs at a constant power level, the hydrogen is cooled by counterflowing cold helium gas. The heater is used in feedback to regulate the hydrogen temperature and compensate for changes in beam intensity.

Given the small emittance of conventional particle beams, liquid-hydrogen targets tend to be narrow transverse to the beam, leading to designs in which the natural direction of hydrogen flow is parallel to the beam. To avoid boiling the liquid in the high-intensity beam core, various design strategems are then necessary to assure transverse flow of the liquid [19, 21]. In contrast, in our flow-through design the hydrogen enters the absorber vessel from below and exits at the top, assuring that the flow is transverse to the beam. The flow pattern is controlled by means of nozzles, which must be configured so as to avoid dead regions or eddies and ensure adequate flushing of the windows.

In the convection design (Fig. 21), the interior wall of the vessel is equipped with cooling tubes through which cold helium gas circulates. A heater located at the bottom of the vessel is used to compensate for changes in beam intensity. The design of the convection-cooled absorber is being guided by two-dimensional fluid-flow calculations carried out at IIT. The flow-through approach is less amenable to calculation but will be tested on the bench to verify the efficacy of the nozzle design, first in a room-temperature model and later at cryogenic temperature. Prototype construction and testing programs for both designs are now underway and will lead to high-power beam tests, currently envisioned for 2002.

2.8.2 Window design

To minimize heating of the beam due to multiple scatering, the absorbers must be equipped with thin, low-Z windows. Yet the windows must be strong enough to withstand the pressure of the liquid hydrogen. We have devised a window design that satisfies these requirements and also allows quite thin absorbers to

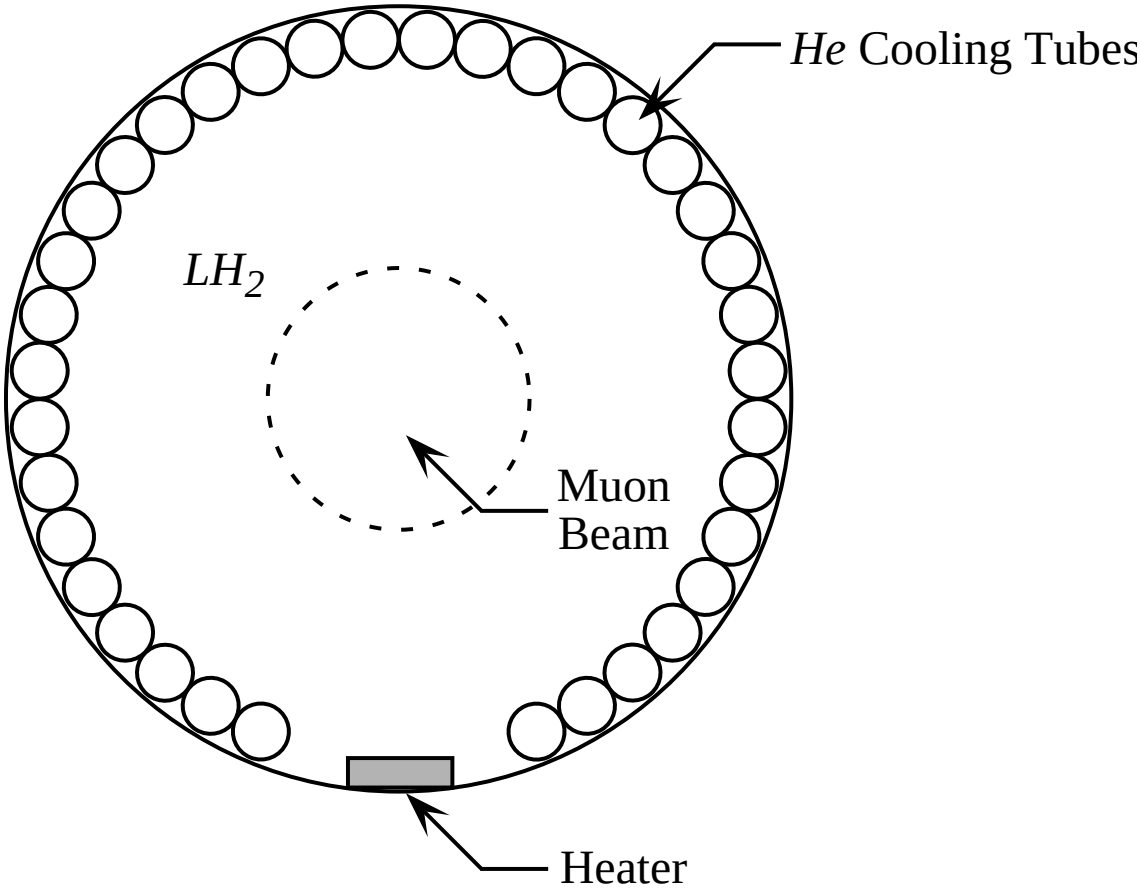

Figure 21: Schematic of convection cooled liquid hydrogen absorber.

be built. While a hemispherical window shape minimizes the window thickness for a given strength, the desire to build absorbers that are thinner relative to their diameter than a sphere leads to the "torispherical" shape. In the version specified by the American Society of Mechanical Engineers (ASME) [23], the torispherical head for pressure vessels is composed of a central portion having a radius of curvature (the "crown radius") equal to the diameter of the cylindrical portion of the vessel, joined to the cylindrical portion by a section of a toroidal surface with a radius of curvature 6% of the crown radius (see Fig. 22).

ASME specifies the minimum acceptable thickness of the torispherical head as

$$t = \frac{0.885PD}{SE - 0.1P}\,, \tag{6}$$

where P is the differential pressure across the window, D the vessel diameter, S the maximum allowable stress, and E the weld efficiency. Although previous high-power liquid-hydrogen targets have operated at 2 atm [18, 19], to keep the windows as thin as possible we have designed for 1.2 atm. For S we follow ASME recommendations and use the smaller of 1/4 of the ultimate strength S_u or 2/3 of the yield strength S_y (in practice, for aluminum alloys it is the ultimate strength that matters). We have decided to machine the window with an integral flange out of a single disk of material (Fig. 23), with the flange fastened to the assembly by bolts (Fig. 24), thus there are no welds and so we take $E = 1$. For 1.2-atm operation, and given the ASME specification for 6061-T6 aluminum alloy $S_u = 289\,\mathrm{MPa}$, we obtain $t = 530\,\mu\mathrm{m}$ for the "lattice 1" absorbers ($D = 0.36\,\mathrm{m}$) and $t = 330\,\mu\mathrm{m}$ for the "lattice 2" absorbers ($D = 0.22\,\mathrm{m}$). However, the windows can be made thinner than this by tapering their thickness as described below. In addition, less easily-machinable, but stronger, aluminum alloys (such as 2090-T81) may allow further reduction in thickness.

In addition to eliminating the weld, machining the window out of a single disk allows detailed control of the window shape and thickness profile. We have used the ANSYS finite-element-analysis program to optimize the window shape and profile so as to minimize the window's thickness in its central portion, where most of the muons traverse it. The resulting shape and thickness profile are shown in Figs. 23.

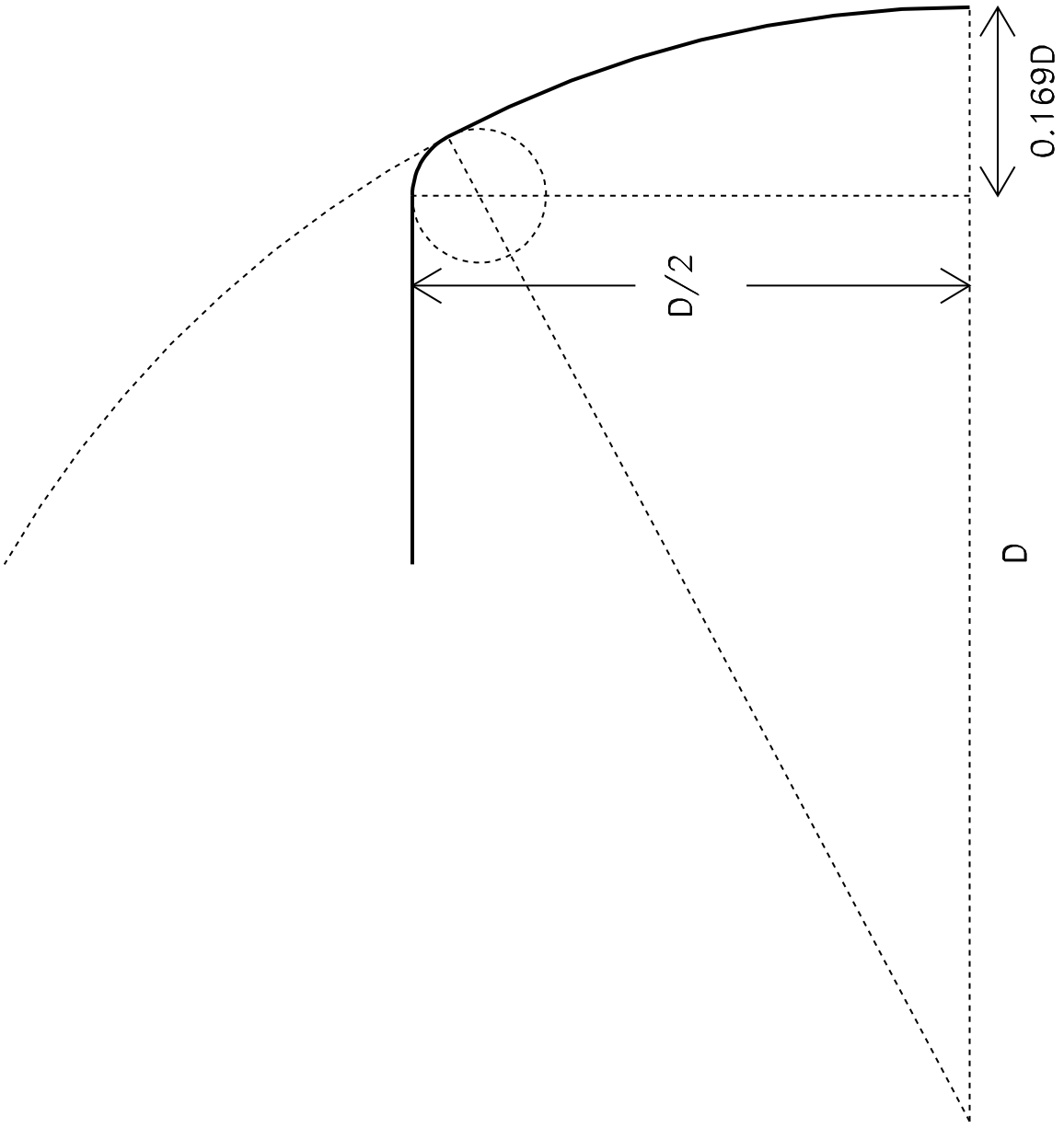

Figure 22: Schematic of ASME torispherical head on cylindrical vessel of diameter D: solid curve shows upper half section, with dashed lines and curves indicating the spherical and toric surfaces from which it is composed.

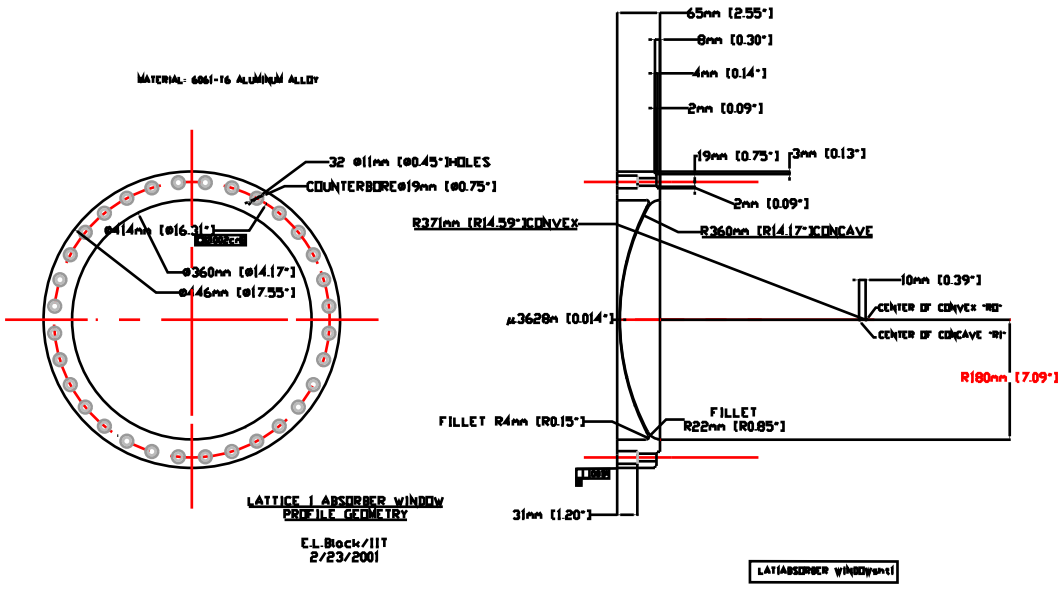

Figure 23: Window design for the sFOFO Lattice 1 absorbers.

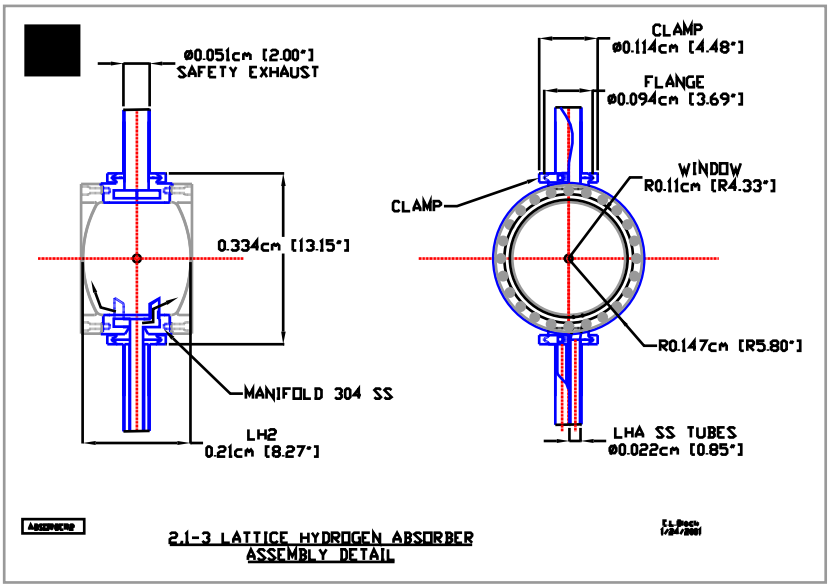

Figure 24: Absorber assembly for sFOFO Lattice 2 (flow-through design shown).

2.9 Instrumentation issues in the Cooling Line

There are a number of unique instrumentation problems involved in optimizing and monitoring the performance the cooling line. The beams will be large and intense, and a variety of precise measurements will be required which are both novel and difficult.

There will be significant backgrounds in all detectors, both due to other particles from the target coming down the line with the muons, and x-rays and dark currents generated by the *rf* cavities. We must consider the angular momentum of the beam, perhaps for the first time any high energy physics beam. The beams will be intense enough so that thermal heating of the detectors will be significant. The environment will have high magnetic fields, a large range of temperatures, and high power *rf* cavities. In addition, under normal circumstances the access will be very limited, since the *rf* cavities and liquid hydrogen absorbers would occupy most of the available space. Loss monitors will not be useful for the low energy muons because the ranges of these particles are so short (6 cm in Cu) and they produce no secondaries.

On the other hand, there are a number of issues that would argue that the tune up and operation could be fairly straightforward. The cooling line has been, and will continue to be, very thoroughly simulated by the time of initial construction. In addition, there are a relatively small number of variables which control the behavior of the beam, such as currents in coils, *rf* parameters and liquid hydrogen target parameters, and these can be measured independently with high precision. While the change in transverse beam emittance, $\epsilon_\perp$, between individual modules may be difficult to measure, $\Delta\epsilon_\perp/\epsilon_\perp < 0.01$, the overall size and profile of a beam with $\sim 10^{12}$ particles is a comparatively straightforward measurement. The high power muon beam considered here makes measurements much easier than for the muon cooling demonstration experiment, which might operate with intensities of only $10^6 - 10^7$ muons.

2.9.1 Tolerances

The sensitivity of the system to alignment errors has been described above. Other concerns are transverse and longitudinal mismatches between the cooling line and the bunching section, arcdown and temporary loss of an *rf* cavity, boiling or loss of hydrogen in the absorber section, or inadvertent introduction of a collimator or thick diagnostic. An R & D program is underway to look at the sensitivity and usefulness of different diagnostic techniques and evaluate them in the environment of *rf* backgrounds and high magnetic fields.

2.9.2 Angular Momentum

Angular momentum plays an important role in solenoid ionization cooling channels, unlike the quadrupole channels used everywhere else in high energy physics. Due to the rotational symmetry of the solenoid focusing field, the canonical angular momentum is a conserved quantity when the cooling material is absent. When absorbers are present, however, the beam angular momentum can change,

thereby yielding a residual angular momentum at the end of a cooling channel. Non-zero beam angular momentum creates coupling between the two transverse degrees of freedom and causes problems for matching the beam into a following quadrupole channel. Furthermore, the angular momentum intrinsically couples with the beam emittance in the cooling dynamics. For efficient cooling in a periodic channel, it is necessary to keep the change in the net angular momentum to be zero. This requirement becomes the following condition[17]

$$\int_0^\lambda \eta(s)\beta(s)B(s)ds = 0 \tag{7}$$

where λ is one period, $B(s)$ is the on-axis magnetic field, $\beta(s)$ is the envelope function, and $\eta(s)$ is the ionization energy loss rate.

Measurement of beam angular momentum is a new subject. A beam profile monitor, which measures beam distribution in x and y, can measure the beam emittance, but does not provide sufficient information to directly determine the angular momentum in a solenoid cooling channel. Based on beam emittance measurements, one may indirectly measure the angular momentum by identifying the two components that have different damping rates in the emittance damping curve. However, such measurements are difficult. Novel ideas are being explored to directly measure the correlation terms $\langle xPy \rangle$ etc.[24]

Since the energy loss rate, absorber thickness, and magnetic field are known, or can be measured with an accuracy much better than one percent, and an envelope function measurement is likely to be accurate to a few percent, it should be easy to determine whether the above requirement is approximately satisfied. Thus for machine operation purposes, beam angular momentum measurement is helpful, but not absolutely necessary. For cooling demonstration experiments, however, good angular momentum measurement can provide further evidence for the cooling behavior. The ability to adjust the amount of material in absorbers is useful for correcting any residual angular momentum at the end of a cooling channel.

2.9.3 Backgrounds

There are a number of distinct backgrounds which will impact beam diagnostics. These backgrounds come primarily from three sources: 1) backgrounds produced by the incident protons at the target, 2) backgrounds produced in the cooling line, primarily from *rf* cavities, and 3) backgrounds from decay electrons. We assume that the decay electrons can be simulated and subtracted from all measurements.

Beam Backgrounds The solenoidal beam transport channel for muons will also transport all other particles whose transverse momentum is less than $\sim$ 100 MeV/c. Thus hadronic showers from 3 GeV protons, for example, can be expected in the liquid hydrogen targets well down the cooling line. A large number of species are produced: K, D, n, γ, $e^{\pm}$, He^3, He^4, and other nuclear

fragments should be seen in detectible quantities. Most low energy backgrounds from the target would be stopped in the first hydrogen absorbers, but the high energy particles which were left would be comparatively uneffected by the *rf* in the line. Timing should be very effective for identifying and discriminating against these particles.

rf **Backgrounds** X ray production from *rf* cavities results from dark current electrons hitting the body of the cavity and nearby solid components. The bremsstrahlung x-ray flux produced is then scattered and attenuated by both the production material and by transmission through any external structure. While the dark current electron orbits would be influenced by magnetic fields along the beam axis, the x-rays, particularly those around 1-2 MeV, would scatter and diffuse freely up and down the cooling line. The dark current electrons from single gap cavities, and the x-rays they produce would be expected to be in the 1 -10 MeV range. The electron and x-ray fluxes produced in this environment have been recently measured in a 1.3 GHz high gradient cavity[26]. Other experiments are planned using an 805 MHz cavity. Data taken from a variety of pulsed cavities seem to imply that *rf* breakdown limits the total dark current and thus the x ray flux that can be produced, somewhat independent of frequency.

Fluxes of dark current electrons and x-rays measured in a 1.3 GHz cavity were on the order of 10^{10} -10^{11} electrons / *rf* pulse, or 10^7 - 10^8 electrons/bucket, a more relevant parameter. The number of bremsstrahlung electrons is of the order $n_e r/L_R$ where r is the dark current electron range, which is usually a few mm, and L_R is the radiation length for the material, 1.44 cm for Cu. Because the energies are low, complex showers do not develop. The photons do, however, diffuse through the system.

There seems to be three ways of altering the flux of dark current electrons and the x-ray flux seen by the beam diagnostics: 1) the geometry of the system can be changed so that dark current electrons do not appear near the beam axis (the single flip cooling channel option does this); 2) the *rf* electric field, E_{rf}, can be reduced since $I_{dark} \propto E_{rf}^{10}$; and 3) the cavity can be coated with an insulating material. All of these are methods are to some extent applicable to the cooling line, so it is difficult at this point to make precise estimates of the radiation flux expected in the beam diagnostics.

2.9.4 Access in the Cooling Line

We assume it will be desirable to be able to insert, park, and also remove any instrumentation in the line without disrupting the beam vacuum. There are a number of options for insertion of diagnostics into the cooling line.

Analogous to FODO accelerator structures, it seems desirable to insert diagnostics at every major focusing element. While there is limited space in the cooling line, it seems that instrumentation modules may be compatible with the 5 - 7 cm expansion section that may be a part of every module, and we have assumed this. Figure 25 shows a possible location for inserting diagnostics in the cooling cell.

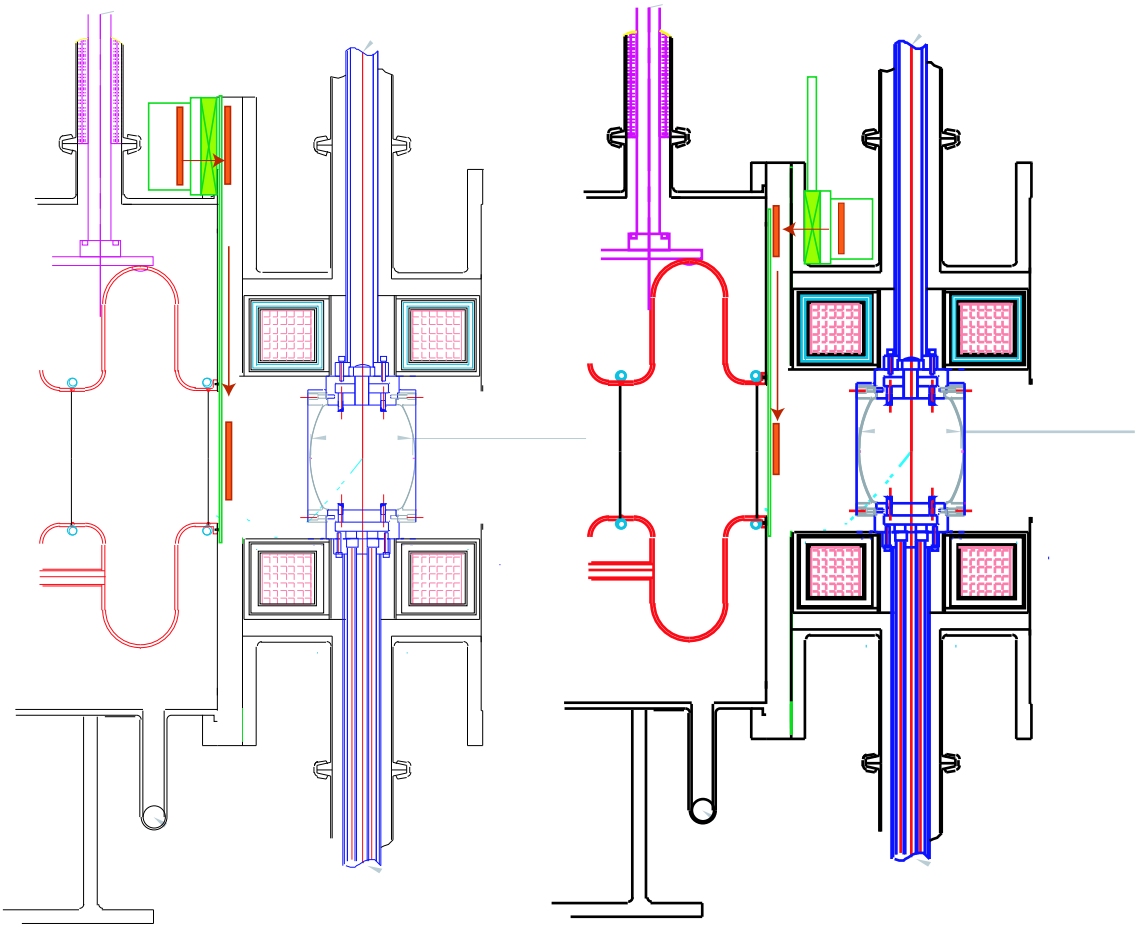

Figure 25: Options for insertion of instrumentation into the cooling line.

Special sFOFO sections, without hydrogen absorbers and with only enough *rf* voltage to contain the bunch, can also be used for specific Cherenkov counters or other devices which require more access than would be available in expansion sections. The expense of these special sections implies that maximum use should be made of the available space in expansion sections.

2.9.5 Making and Using Pencil Beams

We anticipate that pencil beams will be very useful in assessing the alignment of all cooling, accelerator, and storage ring components. Since the range of the 180 MeV/c muons in the cooling line is only about 6 cm in Cu and scattering angles are large, collimation works very well. Thus a variety of collimators could be used at locations in the bunching and cooling lines to produce low transverse emittance beams, on or off axis.

Producing a 6D "pencil" may be even more useful, since this could be used to track the longitudinal evolution of the bunch through all the whole acceleration and storage ring optics. In principle the 6D bunch can be produced from a 4D bunch by reducing the *rf* voltage in the cooling line so that only the center of the longitidinal phase space is transmitted down the line. While the intensities would be reduced, muon beams in the range of 10^{10} to 10^{11}, should be quite easily measured and useful.

2.9.6 Instrumentation Options

Although high energy particles, dark current electrons and x-rays will be present, the primary muon beam should dominate these backgrounds. It seems desirable, however, to look first at instrumentation options which offer very fast time response, so they would be comparatively less sensitive to these backgrounds. From this perspective, Segmented Secondary Emission Monitors (SSEMs) and Faraday cups seem to offer a significant advantage. These devices have been shown to have a useful resolution time of the order of 150 - 200 ps. Since the time response is significantly less than the bucket length, these devices would be able to provide some information on the bunch shape and thus the longitudinal emittance of the beam. Faraday cups could be used essentially interchangibly with the SSEMs. However, they would provide about two orders of magnitude more sensitivity, and the possiblilty of some particle discrimination, using range.

These devices can be used both to measure the beam parameters, but also provide consistency checks for evaluating measurements by other methods. Scintillating fibers, scintillation in the liquid hydrogen, and scintillation counters would also be useful particularly for measurement of the angular momentum of the beam at the end of the cooling line.

Semiconductor arrays of polycrystalline CdTe would be able to provide high precision x and y beam profiles in a single self consistent measurement[25]. The detector consists of an array of charge sensitive elements each providing a signal with amplitude proportional to the intercepted muon beam density.

Likewise bolometers are being developed which can measure xy profiles from the heating in the metallic windows of the liquid hydrogen absorbers. We are also looking at high rate ion chambers, which would be generally useful for a wide range of measurements. Transition radiation, which would detect dark current electrons much more efficiently than muons, may not be useful.

2.10 Tolerances & systematics

The performance of the cooling channel is based on computer simulations using two distinct codes. Yet, some parameters or assumptions in the calculation are identical. As no such channel has been built yet, it is fair to question if the estimation of the cooling performance are robust against small changes in these parameter values. In addition, what are the tolerances on the mechanical alignment in such a long, linear beam transport system? Do we need corrector coils, and if so, where do they need to be placed?

2.10.1 Sensitivity to Multiple Scattering model

ICOOL uses a straightforward Moliere model, imported from the Geant3 package. Geant4 uses an improved version of the Moliere model, but has a tunable parameter. We have studied the sensitivity of the *rms* value of the scattering angle to this parameter, in relation to the known uncertainties in the measured values for these r.m.s. scattering angle for light Z materials. The sensitivity of the μ/P_{15} yield in the relevant range of this tunable parameter has been measured. The systematic error due this uncertainty is approximately 10%.

2.10.2 Control of the energy loss in LH2 and energy gain in the Linac

Because of the relatively narrow momentum acceptance of the channel with respect to the momentum spread due to the large longitudinal emittance, the energy loss and the energy gain, on average, must be known in the channel to better than $\approx 0.25\%$ percent. This tolerance can be achieved in conventional linacs, where the peak voltage and acceleration voltage can be controlled to better than a few tenths of a percent.

The fluctuation in the LH2 density must also be controlled. In order to get a feel for this effect, the LH2 density was randomly set in each absorber, based on a Gaussian model, with a relative σ of 10 % and 20%. The relative μ/P_{15} yield decreased by 5% and 10%, respectively. However, we think that we will be able to keep the density uniform to better than a few percent, based on the experience of the Bates group[19].

The cooling channel will require about 72 12-MW klystrons. It is likely that one, (or more), will fail. One then would empty the most upstream LH2 vessel, and rephase the downstream linacs to keep the beam on the nominal momentum. If a (1,1) or a (1,3) cooling cell has an empty vessel and no *rf* power, after proper rephasing, the performance of the channel degrades by about 5% (relative), allowing us to keep the cooling channel running productively.

2.10.3 Magnet alignments

The design of the cooling channel is being optimized using ideal magnetic fields from cylindrical current sheets[9]-[10]. In an actual magnetic channel, imprecisions that occur in the fabrication and assembly of the solenoids result in mag-

netic fields that deviate from the ideal used in the simulations by some small error field $\delta\vec{B}(x,y,z)$. Typical state-of-the-art magnet construction results in field errors of $\frac{\delta B}{B} \leq 0.1\%$. These field errors produce effects, in general detrimental, that tend to increase with the length of the channel. If left uncorrected, these errors lead to mismatching and betatron oscillations, which in turn result in degradation of the cooling performance of the channel and to a decrease of the channel transmission.

We have considered the following analytical treatment of the detrimental effects of magnet alignment errors. As the muon beam propagates along the periodic channel with a prescribed beta function, it encounters a series of errors of various origins which are assumed to be described by an stochastic function $\delta\vec{B(s)}$ (we neglect the transverse coordinate dependence). The muons experience a series of random forces or *kicks*, which result in a random walk of the centroid of the beam. Statistically, the *rms* magnitude of the transverse deviation $\sqrt{<(\delta x(s))^2>}$ is a function of the length of the channel s. In principle, it should be possible to develop a correction algorithm such that strategically located correction coils bring the centroid back to the ideal trajectory, thereby stopping the deterioration of the cooling process.

A first look at the effects of errors and sensitivity of the present design of the cooling channel has been carried out in references [11] and [12]. Studies of the error fields due to misalignment of individual coils and current sheets are found in references [13],[14].

There are several sources of magnet imperfections that may contribute to the overall deviation from the ideal fields of the channel:

- Geometric survey errors

  1. transverse misalignment of solenoids, characterized by a vector $\vec{d} = d\,(\cos\theta, \sin\theta, 0)$ of magnitude d and direction θ. In the simulations the values of d are chosen from a Gaussian stochastic function.
  2. transverse tilt of full sections of the solenoid characterized by two angles; θ direction with respect to the x-axis, and the tilt by the magnitude ψ with respect to the z-axis.

  The Cartesian coordinates $\vec{r} = (x, y, s)$ transform as

$$\vec{r'} = \vec{r} - \vec{d} \tag{8}$$

  for a translation in the transverse plane and

$$x'_i = \mathcal{M}_{ij} x_j \tag{9}$$

  for a tilted magnet.

  The magnetic fields are calculated as

$$\vec{B}(x,y,s) = \vec{B'}(x',y,s') \qquad B_i(\vec{r}) = \mathcal{M}^{-1}_{ij} B'_j(\mathcal{M}\vec{r}) \tag{10}$$

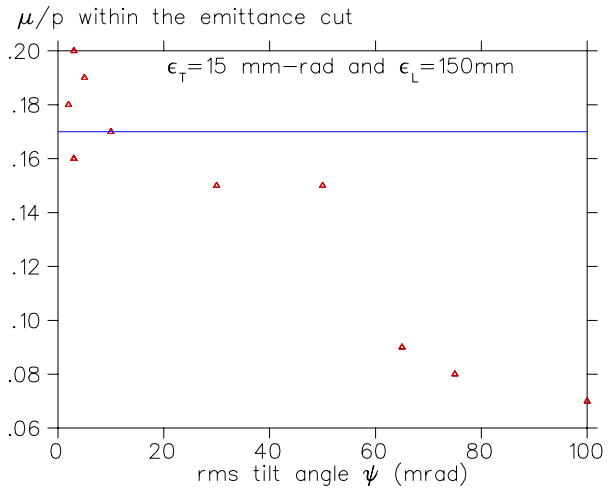

Figure 26: Transmission of the front end for different *rms* tilt angles.

for a translation and tilt respectively. The transformation matrix is

$$\mathcal{M} = \begin{bmatrix} \cos\psi + \cos^2\theta(1-\cos\psi) & \sin\theta\cos\theta(1-\cos\psi) & \sin\theta\sin\psi \\ \sin\theta\cos\theta(1-\cos\psi) & \cos\psi + \sin^2\theta(1-\cos\psi) & \cos\theta\sin\psi \\ \sin\theta\sin\psi & -\cos\theta\sin\psi & \cos\psi \end{bmatrix} \tag{11}$$

- Power supply fluctuations resulting in current fluctuations
- Geometric conductor positioning which leads to random *microscopic* field errors

In this work we only consider the first type, *i.e.*, geometric *macroscopic* field errors introduced by mis-positioning of entire cryostat magnets.

We have performed two studies with ICOOL[5]. The front end baseline has been simulated with independent Gaussian random tilt angles and translation spaced approximately every 5 m. The results are shown in Fig. 26 and Fig. 27.

An independent analysis of this alignment tolerance issue has been done using the generic, 3D Geant4 package. We ran the simulation of the buncher and cooling channels in the following mode:

- Random polar tilts. A Gaussian model was used to generate the "tilts", polar angles ψ, for each coil. This distribution was truncated: θ angles at more than $2\sigma_\theta$ away were resampled. The azimuthal angles were chosen randomly, between zero and 2π (no systematic bias). The μ/p_{15} yield was measured for tens of such simulated channel assemblies. The histogram shown on Figure 28 tells us that a σ_θ of 0.5 mrad gives no statistically significant degradation of the channel performance. However $\sigma_\theta \approx 2.5 mrad$ is unacceptable.

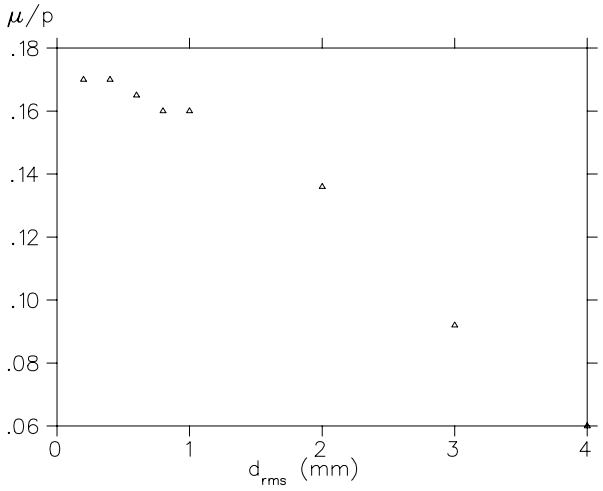

Figure 27: Transmission of the front end for different *rms* translation distance d.

- Random transverse displacements. Since the coils are about 15 cm. long, a tilt of 0.5 mrad gives a lateral displacement at one end of about 75 μm. Evidently, the coil could also shift laterally by about the same amount. We verified that a 2 σ-truncated displacement of 100 μm has no significant impact on the channel performance.

Since the typical tolerance on accelerator magnet's alignment is about 25 to 50 μm, we believe that such a channel can be assembled to the required accuracy. Corrector coils seems to be unnecessary at this point.

2.10.4 Space Charge

The nominal number of muons per bunch is $N_\mu \approx 4/80\times10^{12}$, which corresponds to $Q \approx 8$ nC. An estimate of the deleterious effect on the beam dynamics can be found by calculating the self-electric field of a Gaussian distribution of charge represented by the Basetti-Erskine-Kheifts formula [29]

$$\Phi(r,z,s) = \frac{2Q}{\epsilon_o\sqrt{\pi}}\int_0^\infty dt \frac{e^{-\frac{r^2}{2{\sigma_\perp}^2+t}}}{(2{\sigma_\perp}^2+t)}\frac{e^{-\frac{z^2}{2{\sigma_3}^2+t}}}{\sqrt{(2{\sigma_3}^2+t)}} \tag{12}$$

The variable z is defined as $z = s - c\beta t$ with s the longitudinal coordinate, assuming that the centroid of the bunch is at $s = 0$ at time $t = 0$. The argument s in $\Phi(r,z,s)$ is there to indicate that the *rms* transverse size $\sigma_\perp$ and longitudinal size σ_3 of the beam are functions of s. This is important because the beta function varies from moderate to small values at the absorbers.

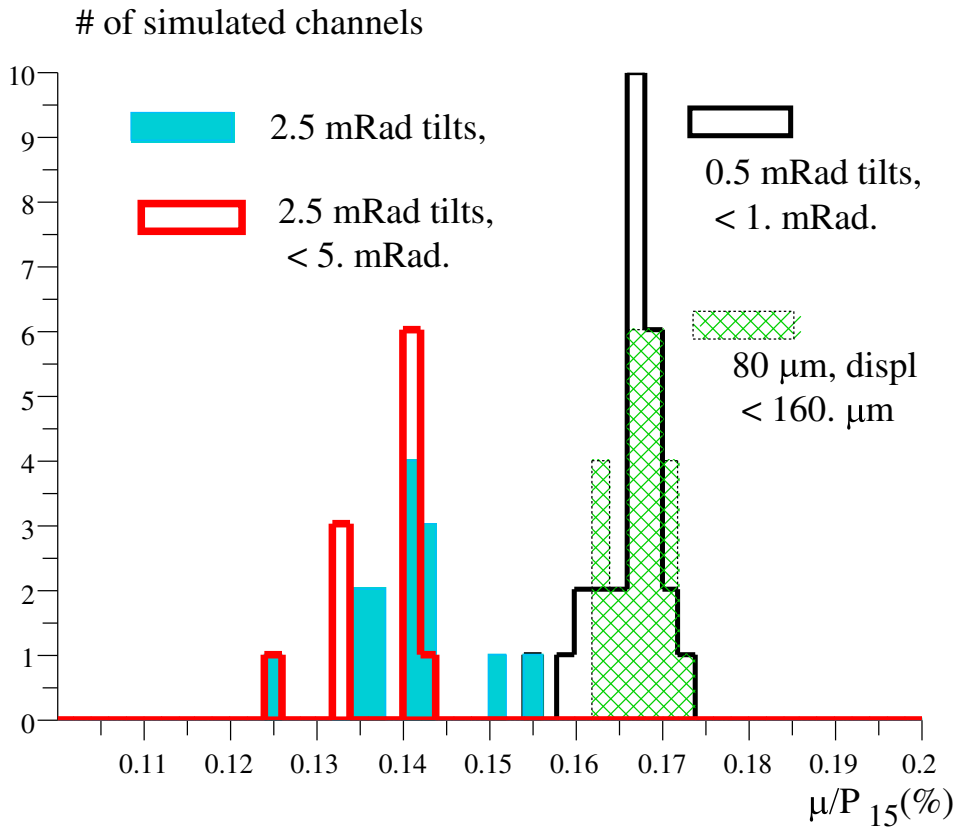

Figure 28: A histogram of the performance of 35 sFOFO cooling channels build with a tolerance of 0.5 mrad tilts. Note that muon decays have been turned off, which explains why the nominal performance is 20.7 %. I'll correct this by rescaling the performance in each run. (PAUL, DOES THIS STILL APPLY?)

From Eq. 12 and the corresponding expression for the vector potential $A_s(r, z, s) = \beta\Phi(r, z, s)$ we can calculate the electric field components $E_r(r, s, t)$ and $E_s(r, s, t)$. [27]

ICOOL contains this formulation and systematic studies have been carried out. The results are shown in Fig. 29, where it can be seen that the number of muon per proton μ/p is rather insensitive to the number of muons in the bunch up to values $N_\mu \approx$ ....

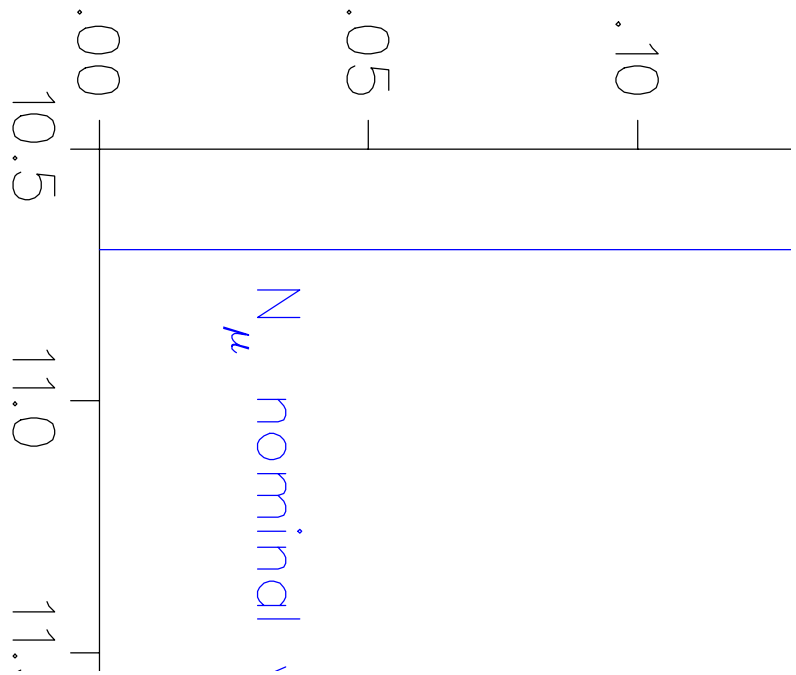

Figure 29: μ/p vs. N_μ in a bunch assuming a Gaussian self-field.

This approach is approximate and leaves aside potentially important phenomena: first the effects of induced charge in the walls of the beam pipe and in the metallic (Be) *rf* windows; second the short range wake potential created by the $\beta < 1$ muon beam inside of the cavities.

The effect of the walls of a cylindrical beam pipe on a bunch of charged particles has been computed with ICOOL. Results are shown in Fig. 30. We can see that for the nominal charge no noticeable effects are detected.

Figure 30: $/mu$/p vs. $N_{/mu}$ in a bunch including the wall effects

The presence of Be windows will mitigate any space charge effects. However,

it is rather difficult to calculate this with precision. Recently, in Ref. [30] it has been shown that MAFIA [**?**] reproduces the theoretical short range wake potentials extremely well for the case of a single particle with $\beta < 1$ in a pill-box cavity. This gives us confidence that MAFIA solutions of the wave equation in the presence of boundary conditions and subluminal particles are correct. Using these fields in ICOOL or GEANT runs will allow a much better evaluation of the space charge problem. In any case, wake fields tend to decrease the effective transverse field seen by the bunch and consequently to reduce the space charge effects.

Next we give some simple arguments to validate the above assertion. The self field E_r causes the beam to expand radially and the corresponding magnetic field focuses the beam. The radial component of the Lorentz force is

$$r'' \approx \frac{qE_r}{mc^2\gamma\beta^2}(1-\beta^2) \tag{13}$$

A long cylinder of radius a and uniform charge density ρ_o creates a field

$$E_r^o \approx \frac{\rho_o}{2\epsilon_o} r \qquad (r < a) \tag{14}$$

Define $\Delta = \frac{<E_r>}{E_r^o}$ with $< E_r >= \int E_r(a,s)ds$ the average of the transverse field at r=a. We can write

$$r'' \approx \frac{qE_r^o}{mc^2\gamma\beta^2}(\Delta-\beta^2) \tag{15}$$

This equation shows that if $\Delta - \beta^2 << 1$ the radial electric field can be reduced by introducing charges in the system, such that their E_r opposes E_r^o and furthermore produces no magnetic field. Indeed, that is the case because of the induced charges in the surface of the metallic windows, which are created to insure that there is no electric field in the bulk of the Be window (perfect conductor approximation) [28]

2.10.5 Engineering "change orders"

Deviation from the design driven by engineering or cost considerations will unavoidably occur. The list below is probably far from complete. We simply mention a few items for the reader to gauge the feasibility aspects of this study:

- Coupling coil configuration. The engineering drawings in Figures 14 and 15 show coils which are shorter and thicker than those described in Table 4. This modification was motivated by ease of assembly and space constraints coming from the *rf* feeds. We verified that such coils perform adequately because they provide a field strength at the center of the half period length consistent with the field shown on Figure 5

- In the design described above, the beryllium *rf* window are "stepped", as their thickness suddenly increases at the radius $r1$ in Table (REFER

TO TABLE 18.D HERE?). A practical implementation could require a smoother distribution of the mass at $r1$ (by chemical etching, for instance). We have verified that a smooth transition would not affect the performance, as expected.

- Absorber shape: The absorbers are not exactly cylindrical, as assumed in the ICOOL simulation. A hyperboloid shape has recently been implemented in Geant4, with no adverse effect to the performance.

- *rf* window shape or configuration. Grids made of aluminum tubes instead of beryllium foils have been proposed. Two concerns come to mind: (i) aluminum has a higher Z than beryllium, and particles can graze the tube surface, (ii) non-uniformity of the electric field around the grid could cause an increase of the beam emittance. We have shown that it is the effective, average radiation length seen by the beam that counts. In particular, if the grid has sufficiently small tube ($\approx$ 2 cm diameter), with large opening between the tubes ($\approx$ 5 to 10 cm), the cooling channel has the same performance as the one equipped with the beryllium foils specified above. The small transverse or longitudinal kicks caused by the grid does not significantly increase the emittance.

- If the downstream accelerator system can really take the 15 mm rad transverse acceptance with no loss, there might not be a strong incentive to cool beyond $\approx$ 100 m, as demonstrated on Fig. 13.

2.11 Conclusion: performance of the entire front-end

The transverse emittance along the entire front-end is plotted in Fig. 31. The emittance is seen to be reduced in the mini cooling at 150 m (from 18 to 13 mm rad), falls a little more as large amplitude particles are lost in the induction linac, and falls fast in the final cooling (from 12 to 2.2 mm rad).

The muons per proton along the full system are given in Fig. 32. The particle losses prior to the buncher come primarily from the loss of very high and very low momenta (about 30 %), plus (approx 20 %) loss from muon decay . The losses in the cooling come ≈25% from bunching inefficiency and ≈25% from loss of particles from the *rf* bucket as the longitudinal emittance grows in the cooling.

Fig. 33 shows the distributions of initial pion energies for (upper curve) all pions exiting the target and (lower curve) those pions that decayed to muons and exited the cooling. The second figure gives the ratios of these two and indicates that at the peak about 35 % of the pions yield muons at the end. Note the falling efficiency for higher energy pions.

The sFOFO cooling channel increases the number of muons per proton in the 15 mm rad transverse aperture by a factor 3.5, or a factor 5.75 in the 9.75 mm rad aperture (Geant4 estimate, ICOOL numbers listed above are a bit lower, consistent with systematic errors in the calculations). The corresponding number for the FOFO channel used in Feasibility Study I was approximately 2 to 2.5 [1]. Engineering and mechanical tolerances have been studied. We now know that such a channel can be assembled and aligned with known techniques. Finally, no new R& D programs beyond those defined a year ago[1] are required.

References

[1] "A Neutrino Source Based on an Intense Muon Storage Ring", ed. N. Holtkamp and D. Finley, submitted to Phys Rev. ST Accel. Beams (2000), available at http://www.fnal.gov/projects/muon_collider/nu-factory/nu-factory.html

[2] C.M. Ankenbrandt *et al* Phys. Rev. ST Accel. Beams 2, 081001 (1999)

[3] G. Penn *et al* Phys. Rev. Lett. 85 (4) pp. 764-767. July, 2000.

[4] J. Monroe *et al Design and Simulation of Muon Ionization Cooling Channels for the Fermilab Neutrino Factory Feasibility Study*, submitted to Phys. Rev. ST Accel. Beams.

[5] R. Fernow *et al*, "ICOOL, A Simulation Code for Ionization Cooling of Muons Beams", Proceedings of the 1999 Particle Accelerator Conference, A. Lucio and W. MacKay, eds. (IEEE, Piscataway, NJ, 1999) p. 3020.

[6] The Geant4 Tool Kit is available at *http://wwwinfo.cern.ch/asd/geant4/geant4.html*

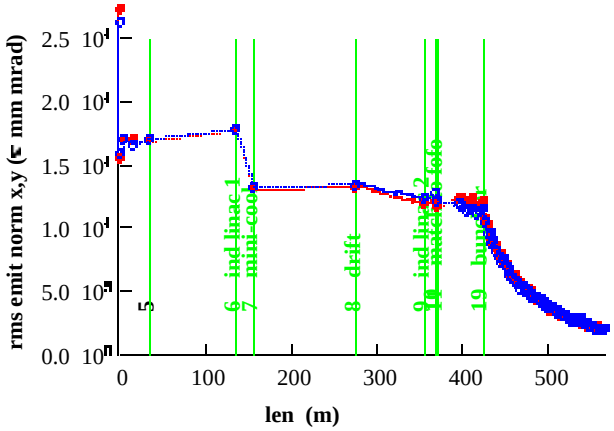

Figure 31: Emittance as a function of distance along the front end.

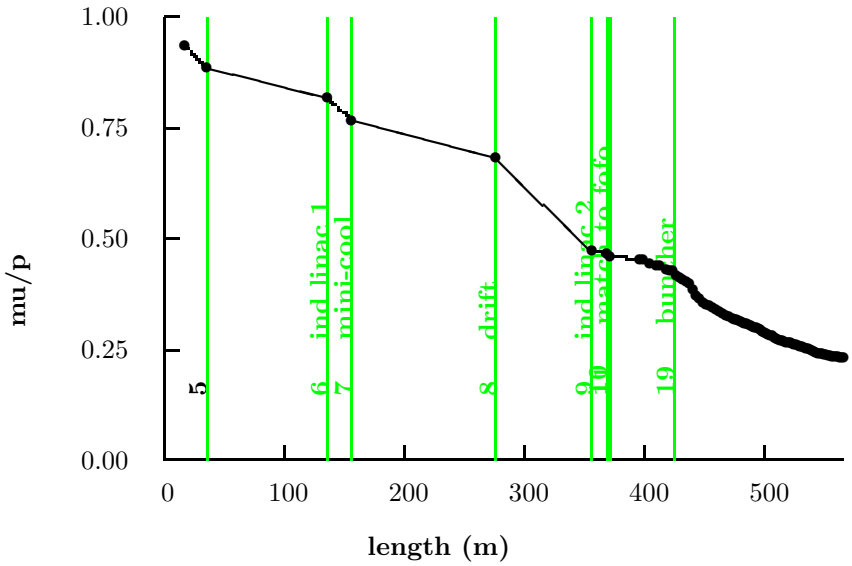

Figure 32: Muons per incident proton as a function of distance along the front end.

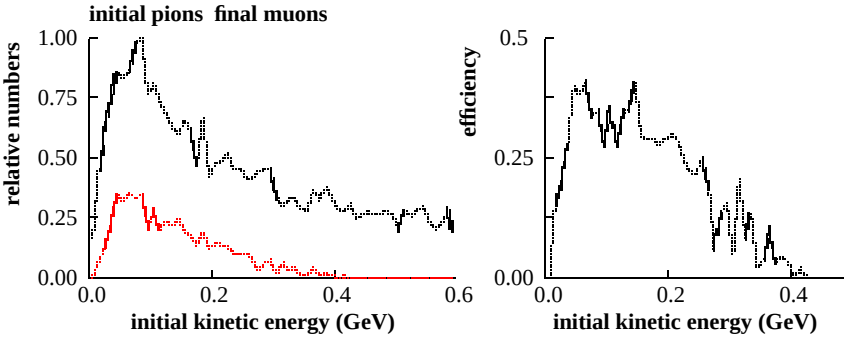

Figure 33: Initial kinetic energy of produced pions and muons exiting the cooling section.

[7] This code was written by G. Penn, LBNL.

[8] The Particle Data Group, *Review of Particle Physics*, EPJ C **15** p. 163 (2000)

[9] B. Palmer, *Neutrino Factory Draft Parameters*
http://www-mucool.fnal.gov/mcnotes/muc0046.ps

[10] Jocelyn Monroe, Paul Lebrun, Panagiotis Spentzouris, *DPGeant and Icool Code Comparison*
http://www-mucool.fnal.gov/mcnotes/muc0072.ps

[11] R. Fernow, *Effect of a dipole error on the performance of the alternating solenoid lattice*
http://www-mucool.fnal.gov/mcnotes/muc0035.pdf

[12] Paul Lebrun, *Sensitivity of the 15 T. Alternate Solenoid Cooling Channel to Dipole Errors caused by misalignment of the Solenoids*
http://www-mucool.fnal.gov/mcnotes/muc0073.ps

[13] Juan C. Gallardo, *Errors in a continuous solenoid* ,
http://www-mucool.fnal.gov/mcnotes/muc0041.ps; *Errors in a discrete solenoid*
http://www-mucool.fnal.gov/mcnotes/muc0037.ps

[14] Juan C. Gallardo, *Note on Vector potential for a Solenoid and Errors*, unpublished.

[15] First suggested by A. Sessler, LBNL.

[16] Semertzdis and Morse, Unpublished Note BNL 2000

[17] [Kwang-Je Kim and Chun-xi Wang, PRL 85 (760) 2000]:

[18] J. W. Mark, SLAC-PUB-3169 (1984) and references therein.

[19] E. J. Beise *et al.*, Nucl. Instrum. Meth. **A378** (1996) 383.

[20] R. W. Carr *et al.*, SLAC-Proposal-E-158, July 1997.

[21] R. W. Carr *et al.*, "E158 Liquid Hydrogen Target Milestone Report," April 21, 1999, http://www.slac.stanford.edu/exp/e158/documents/target.ps.gz.

[22] D. J. Margaziotis, in *Proc. CEBAF Summer 1992 Workshop*, F. Gross and R. Holt, eds., AIP Conf. Proc. **269**, American Institute of Physics, New York (1993), p. 531.

[23] "ASME Boiler and Pressure Vessel Code," ANSI/ASME BPV-VIII-1 (American Society of Mechanical Engineers, New York, 1980), part UG-32.

[24] A. Blondel is working to develop a system based on a ring imaging Cerenkov technique.

[25] M. Placidi *et al.*,"A CdTe Detector for Muon Transverse Profile Measurements", CERN-NUFACT-Note 068, Contributed to the MuCool Instrumentation Workshop, IIT, Chicago, Nov,10-11, 2000.

[26] X-RAY STUDIES REFERENCE HERE

[27] SPACE CHARGE REFERENCE HERE

[28] SPACE CHARGE REFERENCE HERE

[29] SPACE CHARGE REFERENCE HERE

[30] SPACE CHARGE REFERENCE HERE

[31] SPACE CHARGE REFERENCE HERE